Review

Not peer-reviewed version

Plasma-Sprayed Osseoconductive Hydroxylapatite Coatings for Endoprosthetic Hip Implants: Phase Composition, Microstructure, Properties, and Biomedical Functions

ROBERT Bertram Heimann *

Posted Date: 23 May 2024

doi: 10.20944/preprints202405.1476.v1

Keywords: Hydroxylapatite; coatings; plasma spraying; implants; functions; properties

Preprints.org (www.preprints.org) | NOT PEER-REVIEWED | Posted: 23 May 2024 doi:10.20944/preprints202405.1476.v1

Review

Plasma-Sprayed Osseoconductive Hydroxylapatite Coatings for Endoprosthetic Hip Implants: Phase Composition, Microstructure, Properties, and Biomedical Functions

Robert B. Heimann

Am Stadtpark 2A, D-02826 Görlitz, Germany; robert.heimann@ocean-gate.de

Abstract: This contribution attempts to provide a state-of-the-art account on the physicochemical and biomedical properties of plasma-sprayed hydroxylapatite (HAp) coatings that are routinely applied to the surfaces of metallic endoprosthetic and dental root implants, designed to replace or restore lost functions of diseased or damaged tissues of the human body. Even though the residence time of powder particles of HAp in the plasma jet is extremely short, the high temperature applied introduces compositional and structural changes of the precursor hydroxylapatite that severely affect its chemical and physical properties and in turn, its biomedical performance. These changes are based on the incongruent melting behaviour of HAp and can be traced, among many other analytical techniques, by high-resolution synchrotron X-ray diffraction, vibrational (Raman), and nuclear magnetic resonance (NMR) spectroscopies. *In vivo* reactions of the plasma-sprayed coatings with extracellular fluid (ECF) can be assessed and predicted by *in vitro* testing using simulated body fluids as proxy agents. Ways are being discussed to safeguard appropriate biological performance of hydroxylapatite coatings in long-term service by controlling their phase content, porosity, surface roughness, residual stress distribution, and adhesion to the implant surface.

Keywords: Hydroxylapatite; coatings; plasma spraying; implants; functions; properties

---

1. Introduction

The worldwide need and increasing demand for endoprosthetic hip and knee implants is deeply rooted in the kinematics of human locomotion. The loads exerted on the hip and knee joints are roughly one time the body mass during rest (~ 1 kN), two to three times the body mass during normal walking, up to five times when jogging, and up to eight times during jumping. Beyond this threshold, the risk of irreversible joint damage increases drastically. Intensifying the socio-economic impact of this physiologically given situation is the fact that people generally live longer and gain weight by overeating, and excessive consumption of sugar, fat, and alcohol, combined with lack of exercise. Eventually, the protective cartilage tissue wears away that lines the femoral head and the acetabular cup of the hip joint. This leads to increased friction during movement, and in turn to inflammation, pain and, finally, immobilization. Common root causes for the need of hip joint replacement are osteoarthritis, rheumatoid arthritis, osteonecrosis, injuries or broken bones from trauma or disease, and degeneration due to wear and tear. In all these cases, a THA (total hip arthroplasty) is the only reasonable option to restore mobility and hence, to promote a rewarding life without pain. This type of operation has a long pedigree, starting with the pioneering work by Themistocles Gluck (1853-1942) and continuing with Robert Judet (1909-1980) and Austin T. Moore (1899-1962) to Sir John Charnley (1911-1982), who designed the hip joint replacement system on which all subsequent solutions are based.

Figure 1A shows a state-of-the-art THA endoprosthesis for cementless use, consisting of a hydroxylapatite-coated titanium alloy stem with an alumina femoral ball attached that will be anchored in the femur, and an acetabular cup with an alumina inset anchored in the hip bone. In the absence of lubricating hyaluronic acid-based synovial fluid, this type of ceramic-on-ceramic (CoC) bearing couple is highly effective and reliable, even though it may suffer from disturbing squeaking noise during walking and a high risk of fracture [1]. In addition, its comparatively high cost puts a severe strain on the healthcare systems of many countries. Hence, for economic reason, the standard endoprosthesis does not use the bearing couple option shown in Figure 1A but that of a ceramic (CoP) or metal (MoP) femoral head articulating against a highly cross-linked polyethylene-lined acetabular cup. Figure 1B shows the cross-sectional image of the implant-bone interface, demonstrating that a plasma-sprayed hydroxylapatite (HAp) layer provides a thigh and continuous connection between an implant and bone [2].

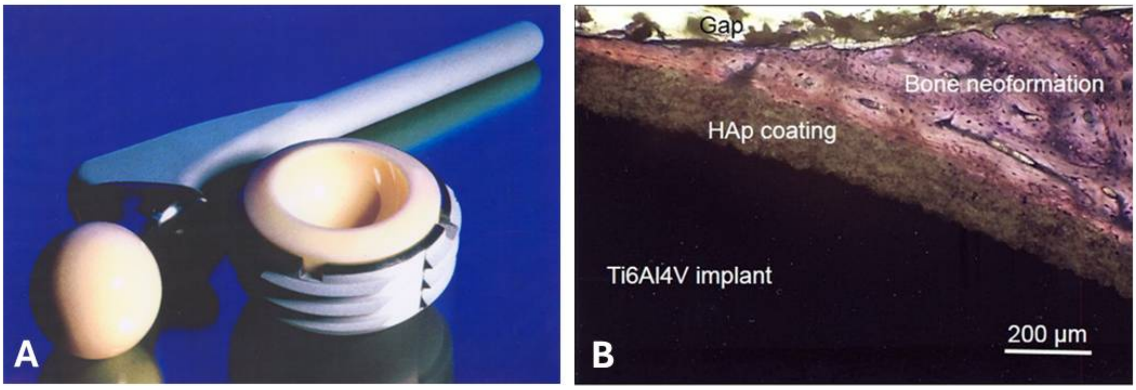

Figure 1. A: High-end total hip endoprosthesis consisting of the femoral Ti6Al4V stem with an alumina femoral ball (left) and a titanium acetabular cup with an alumina insert (right). Note the white plasma-sprayed HAp coating of the stem and the acetabular cup casing. Image courtesy Professor Gerd Willmann †, CeramTec AG, Plochingen, Germany. **B**: As shown in this cross-section, a plasma-sprayed HAp coating provides a tight and continuous connection between a Ti6Al4V implant and newly formed cortical bone matter. Sample stained with toluidine blue [2]. © With permission by Springer Science and Business Media.

Not surprisingly, total hip (THA) and knee arthroplasty (TKA) are among the most frequently performed and in their long-term outcome highly successful and effective surgeries worldwide. In 2022, some 3.1 million THA and TKA procedures were reported in the USA alone, among them 37% primary THA and 54% primary TKA, the remainder being revision operations [3]. In 2021, ceramic-on-polyethylene (CoP) bearing couples were with about 63% the dominant choice for THA. Cementless fixation of the femoral stem constituted about 95% of all THA, in contrast to only 19% of all TKA.

In Germany, about 178,000 primary THA and 137,000 primary TKA were registered in 2022, whereby 58% of all THAs were performed with a ceramic-on-polyethylene (CoP) sliding couple [4]. Most other remaining implants used a metal-on-polyethylene (MoP) combination. Some 10% of all hip operation surgeries were revisions, the causes of which were, in descending order, implant loosening (23%), periprosthetic infection (16%), post-operative periprosthetic fracture (16%), dislocation (14%), wear (6%), and others (24%). Purely mechanical implant failure was remarkably low in only 2% of all THA revision operations, attesting to the high reliability and solidly entrenched quality standards of modern biomedical devices and operation techniques. Indeed, the revision probability after 5 years post-implantation was found to be only around 4%. In a global context, in Switzerland, Germany and Austria, the number of THAs performed were a high 3230/1 million population (ppm), 3010 ppm, and 2870 ppm, respectively, compared to only 400 ppm in Chile, 180 in Costa Rica, and a paltry 70 ppm in Mexico. In 2021, the THA average of all OECD countries was 1720 ppm [4].

The high incidence of THA and TKA operations in the developed and increasingly, in the developing world, is reflected in the global hip replacement implant market valued at USD 7.26 billion in 2022, expected to grow at a CAGR of 5.2% to USD 11.5 billion in 2031[5]. Hence, hip and knee arthroplasties constitute a meaningful part of the global GNP. This is also mirrored by the growing number of research and development effort designed to improve existing and discover novel solution for the growing demand of endoprosthetic devices. Several aspects of this research effort will be discussed in this contribution.

2. Why Hydroxylapatite Coatings?

As shown in Figure 1A, modern endoprosthetic implants are coated frequently with a thin layer of hydroxylapatite (HAp) that assists in tight and continuous osseointegration (Figure 1B). HAp-coated cementless implants are still considered the current 'gold standard' in hip arthroplasty and dental restoration. The reason for this is grounded in the chemical and structural similarity of synthetic HAp with biological, *i.e.* bone-like apatite (bone mineral), making HAp a highly biocompatible material. Nevertheless, although synthetic HAp noticeably differs in its chemical composition, stoichiometry, crystalline order, defect density, hydroxyl ion content, and type and degree of ion substitution from bone mineral, in biomedical application it spans the wide range from hip and dental root implant coatings, porous bone-growth supporting 3D-printed scaffolds to bone cavity filling material, and drug and gene delivery vehicles.

Any foreign material or device incorporated into the body trigger a host/recipient response that manifests itself in the five time-dependent foreign body reaction (FBR) phases, *i.e.*, (i) blood protein adsorption completed in a few seconds after contact, (ii) neutrophil recruitment and associate acute inflammation within minutes, (iii) monocyte recruitment and their differentiation to macrophages, associated with chronic inflammation within hours, (iv) foreign body multinucleated giant cell formation after some days, and (v) fibrotic encapsulation within weeks. The formation of a fibrous connective tissue capsule around the implanted biomaterial (Figure 2A) is a protective measure of the body, but unfortunately prevents solid and lasting osseointegration of the implant.

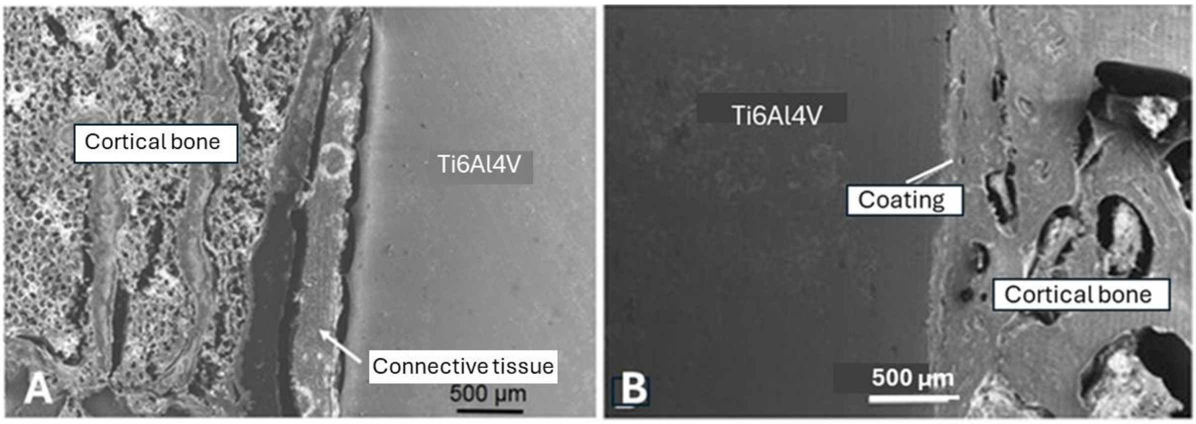

Figure 2. A: Formation of an acellular connective tissue capsule as a typical foreign body reaction (FBR) around a Ti6Al4V cube (5 x 5 x 5 mm^3) implanted into the femoral condyle of an adult dog for 6 months [6]. **B**: Absence of an acellular connective tissue capsule and tight osseointegration of a Ti6Al4V cube implanted into the lateral condyle of a dog femur for 6 months in the presence of a thin plasma-sprayed HAp coating [6]. © With permission by Wiley-VCH.

The fibrous encapsulation of the implanted device can affect implant function and leads frequently to failure. For example, interface loosening of a press-fitted implant may be caused by mechanically induced periprosthetic osteolysis, in particular when associated with micro-movements of the patient during the healing phase that limits implant longevity. Such early loosening is best defined as prosthetic migration. Initiation of loosening during or shortly after surgery is promoted by poor implant interlock, poor bone quality, and osteolytic resorption of a necrotic bone bed.

The quest for reducing the FBR is an effective way to promote better implant performance and longevity, including enhanced adhesion and strengthening of the implant-bone interface. Among many possible ways to combat FBR [7], coating the implant stem and the casing of the acetabular cup of a hip joint implant with a thin layer of osseoconductive HAp (Figures 1A, 2B) is an economically viable and biomedically reliable route towards alleviating the FBR and thus, preventing the formation of a fibrous connective tissue capsule. Recast in simple terms, a HAp coating acts as an agent of biological subterfuge, triggering the body into accepting the implant as part of its own metabolic environment, thus avoiding the negative consequences of FBR.

In addition to preventing formation of a fibrous acellular connective tissue capsule surrounding the implant, other advantages of a plasma-sprayed HAp coating include:

- enhanced bone apposition rate by osseoinduction, owing to preferential adsorption of bone growth-supporting factors such as bone morphogenetic proteins (BMPs) and non-collagenous proteins (NCPs) such as osteocalcin, osteonectin, silylated glycoproteins, and proteoglycans,
- enhanced bonding osteogenesis that provides a strong and continuous interface between bone tissue and implant, and thus, enables to transmit not only compressive but also (limited) tensile and shear forces,
- variable HAp coating thickness between 50 and 250 µm can be selected, dependent on application; novel deposition techniques such as suspension plasma spraying (SPS) or solution precursor plasma spraying (SPPS) allow depositing coatings with thickness << 50 µm when required,
- acceleration of the healing process when compared to implants without an osseoconductive coating,
- supporting attachment of epithelium in case of transmucosal dental implants,
- reduced risk of release of potentially toxic heavy metal ions from the implant to the periprosthetic tissue and thus, minimizing a possible cytotoxic response, and
- quality control and standards according to ASTM F1185-03 (2014), ASTM F1044-05(2017), ASTM F1160 (2014), ISO 13179-2: 2018, and others.

However, despite the fact that modern endoprosthetic hip joint implants have reached a high degree of mechanical resilience, chemical inertness, biocompatibility, and overall performance reliability as manifest in a high Weibull modulus, safeguarding their long-term successful behavior in the aggressive environment of the human body remains a major challenge. Stability problems may be associated with so-called aseptic loosening long after surgery that to some degree can be related to the large gradient of the modulus of elasticity of the metallic implant (around 110 GPa for Ti6Al4V) and cortical bone (10-15 GPa). Mechanical loads will then be transmitted through the high modulus metal implant rather than through bone matter, causing the latter to atrophy by forced bone mass loss since bony health depends strongly on continuous tensile loading and bone remodelling along Wolff's law. This mechanism is known by the term of 'stress shielding'. Modern ß-type Ti alloys with elastic moduli closer to bone such as Ti29Nb13Ta4.6Zr (TNTZ) with a modulus < 60 GPa are thought to reducing the risk of stress shielding.

In parallel, the very process of plasma spraying triggers large tensile quenching and thermal stresses at the interface and throughout the bulk coating that subsequently in medical service may result in chipping and even delamination of the osseoconductive HAp coating layer. The reason underlaying residual stresses are manifold but all related to differences in the coefficients of thermal expansion between the metallic substrate and the ceramic coating (see Section 5.3.8).

A possible way to avoid this to happen is the application of bond coats that act as intermediates, binding both implant and HAp coating tightly to cortical bone matter [8]. In addition, such titania or zirconia bond coats are thought to function as thermal barriers, able to reducing the steep gradient of the coefficient of thermal expansion between metallic implant and ceramic coating. They decrease the rate of heat transfer and thus, the degree of thermal decomposition of HAp during plasma spraying and aid in reducing the occurrence of amorphous calcium phosphate (ACP) formed by a quenching contact at the immediate coating-substrate interface. However, despite their clear advantages, in the clinical praxis no bond coat of any nature has been applied to endoprosthetic implants yet. Consequently, to date, their biomedical potential, although promising, has been only experimentally tested and assessed in animal models.

3. A Short History of Calcium Orthophosphate Research

The close association of calcium phosphates with living matter such as bone has been known for a rather long time. Calcium orthophosphates including hydroxylapatite, $Ca_{10}(PO_4)_6(OH)_2$ were known to be associated with organic tissue, more specifically with bone, for at least 250 years [9].

Early evidence points to 1769, when the Swedish chemists Johan Gottlieb Gahn (1745-1818) and Carl Wilhelm Scheele (1742-1786) found tricalcium orthophosphate, $Ca_3(PO_4)_2$ to be the product of burning bone.

Subsequently, the presence of calcium orthophosphates in bone, teeth, and pathologic urinary and renal calculi was solidly established by the early nineteenth century. Some calcium phosphate phases involved in biomineralization such as amorphous calcium phosphate, octacalcium phosphate, and dicalcium phosphate dihydrate (brushite) [10] were already known or suggested by the end of the nineteenth century.

However, only the application of X-rays to crystal structure analysis over one hundred years ago [11] allowed a paradigmatic shift from a descriptive to a predictive acquisition of information on the structural chemistry of biological calcium phosphates [12–16]. Willem F. de Jong [17] was first to identify the structure of the calcium phosphate phase in bone as being akin to geological apatite, and in turn, Hendricks et al. [12] concluded (erroneously) that the inorganic constituent of bone contains carbonate apatite, $Ca_{10}[CO_3(PO_4)_6]\cdot H_2O$, thought to be structurally equal to fluorapatite. The same authors mentioned oxyapatite, $Ca_{10}O(PO_4)_6$ as an anhydrous product of heating HAp up to 900°C. This was disputed by Bredig and coworkers [16] who instead, proposed the existence of only partly dehydroxylated oxyhydroxylapatite (OHAp), $Ca_{10}(PO_4)_6X_{2m}O_n$ ($X = OH^-$; $m + n = 1$). In their opinion, an empty X site would destabilize the structure, a contention that was much later confirmed by computer modelling applied to investigate the dehydration of HAp to oxyapatite (OAp) and the defect chemistry of calcium-deficient HAp [18]. However, despite these thermodynamically based constraints, there is evidence that under certain experimental conditions, OAp can be stabilized [19–22] (see Section 5.3.5).

A thorough account on the chemical composition and structure of bone mineral, *i.e.*, Ca-deficient HAp with the approximate formula of $Ca_{10-x}(HPO_4)_x(PO_4)_{6-x}$ $(OH, O, Cl, F, CO_3, \square)_{2-x}\cdot nH_2O$; $0<x<1$; $n = 0\text{-}2.5$ [23,24] was given in a review by Rey et al. [25] and the role that water molecules play in the structure of bone was highlighted by Pasteris [26]. More details on the structure and biological function of biological apatite can be extracted from Ref. [8].

4. Hierarchical Structure of Bone

The realization that calcium orthophosphates are crucial constituents of bone matter has led eventually to their application in several medical disciplines. A major segment of utilization of the calcium orthophosphate HAp is the challenging fields of bone reconstruction, bone scaffolds, coatings for hip, knee and dental implants, and vertebrae replacement [27].

The structure of bone can be regarded as a biocomposite consisting of Ca-deficient defect biological HAp nanocrystals of about 30 x 50 x 2 nm^3 size, orientationally intergrown with triple helical strands of matrix proteins such as collagen I (ossein). Consequently, a spatially hierarchical organization exists that forms the basic structural units of bone [28,29]. Figure 3A shows schematically the hierarchical architecture of bone microfibrils [30], and Figure 3B shows a molecular mechanics model of the oriented intergrowth of hydroxylapatite nanocrystals with tropocollagen fibers at different degrees of mineralization (0 to 40%) [31].

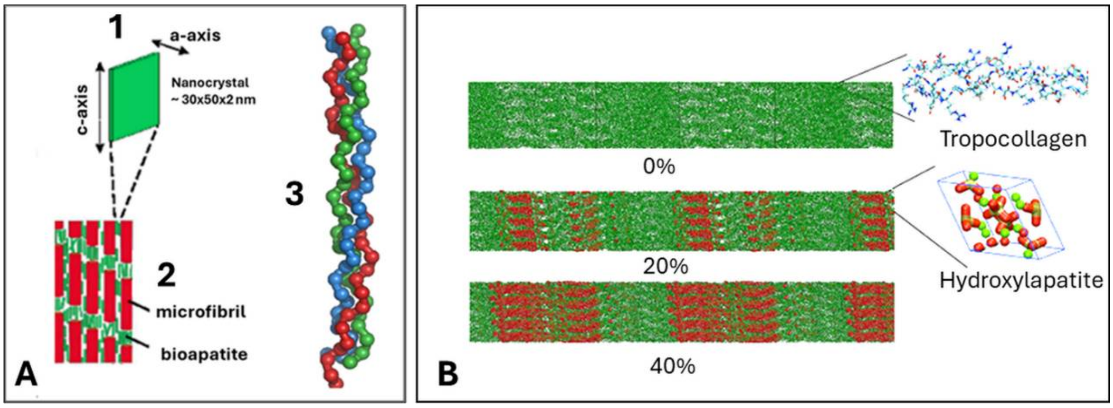

Figure 3. A: Schematics of the hierarchical nano-architecture of cortical bone, showing an individual crystalline platelet of HAp (1), an array of five collage microfibrils with oriented intergrown HAp

nanocrystals that constitutes the smallest organic structural unit of the bone (2), and a triple helical strand of tropocollagen consisting of three polypeptide α-chains (3). Image modified after Ref. [30]. © Permission granted under Creative Commons Attribution 4.0 International License. **B:** Collagen microfibril model with different degrees of mineralization The HAp crystals are arranged such that their c-axes align with the fibril axis [31]. © Permission granted under Creative Commons Attribution-NC ShareAlike 3.0 International License.

5. Osseoconductive Hydroxylapatite Coatings

Given the important role that HAp coatings applied to the surface of an endoprosthetic implant play, it is not surprising that almost 50 years ago synthetic HAp was suggested as a biocompatible artificial material for incorporation in the human body [32]. Soon after, HAp was deposited as a bioactive, *i.e.*, osseoconductive coating on dental implants, followed by coating the stem of endoprosthetic hip implants to improve implant integration with the surrounding bone [33].

5.1. Osseoconduction, Osseoinduction, and Osseointegration

Osseoconduction refers to the ability of a biocompatible material such as hydroxylapatite to support the in-growth of bone cells, blood capillaries, and perivascular tissue into the operation-induced gap between implant and the existing cortical bone bed [27]. The process results in a bony surface with various channels, pores, and a matrix that provides a scaffold for the newly formed bone matter.

The term *osseoinduction* refers to the recruitment of immature cells and their stimulation to develop into preosteoblasts [34]. Hydroxylapatite-based bioactive implant coatings promote normal differentiation in surrounding tissues by providing a fertile environment for enhanced cell adhesion. Cytoskeletal microfilaments such as actin, myosin, actinin, and tropomyosin that control cell shape and migration will be coupled through specialized cell membrane proteins (integrins) to extracellular adhesion molecules such as fibronectin, laminin, vitronectin, or thrombospondin. An interfacial layer of hydroxylapatite will adsorb these integrins in a favorable conformation and promote the formation of focal adhesion centers. Particular growth factors (cytokines) may also be recruited and adsorbed at specific hydroxylapatite surface sites, thus further promoting osseoinduction. These growth-supporting cytokines include transforming growth factor-β, insulin-like growth factor-1, tumor necrosis factor-α, or recombinant human bone morphogenetic proteins (rhBMPs) that all provide a degree of osseostimulation, supporting the transformation of undifferentiated mesenchymal precursor cells into osteoprogenitor cells preceding endochondral ossification.

Finally, *osseointegration* describes the process by which interfacial bone is formed between an inorganic implant and living bone as a defence reaction akin to FBR. It is characterized by the firm anchoring of a surgical implant by the growth of bone around it without fibrous tissue formation at the interface [34]. When an implant is osseointegrated, there is no progressive relative movement between it and the bone with which it is in direct contact. This means that osseointegration is the requirement for the desired long-term stability of an endoprosthesis.

5.2. Deposition Techniques

A plethora of techniques are available and used to apply HAp coatings that can be divided into non-thermal and thermal methods. Non-thermal methods carried out at or near ambient temperature include biomimetic deposition, electrochemical (ECD) and electrophoretic deposition (EPD), sol-gel deposition by dip and spin coating, hydrothermal deposition, and radiofrequency magnetron sputtering (r.f.MS). Thermal methods include atmospheric (air) plasma spraying (APS), micro-plasma spraying (MPS), low energy plasma spraying (LEPS), low pressure (vacuum) plasma spraying (LPPS/VPS), suspension plasma spraying (SPS), solution precursor plasma spraying (SPPS), plasma electrolytic oxidation (PEO), pulsed laser deposition (PLD), and other less frequently utilized techniques such as cold gas dynamic spraying (CGDS), flame spraying (FS), high velocity suspension flame spraying (HVSFS), high velocity oxyfuel spraying (HVOF), and chemical vapour deposition (CVD) [8].

The preferred deposition method of biomedical hydroxylapatite was and still is atmospheric plasma spraying [8,27,35–37] (Figure 4).

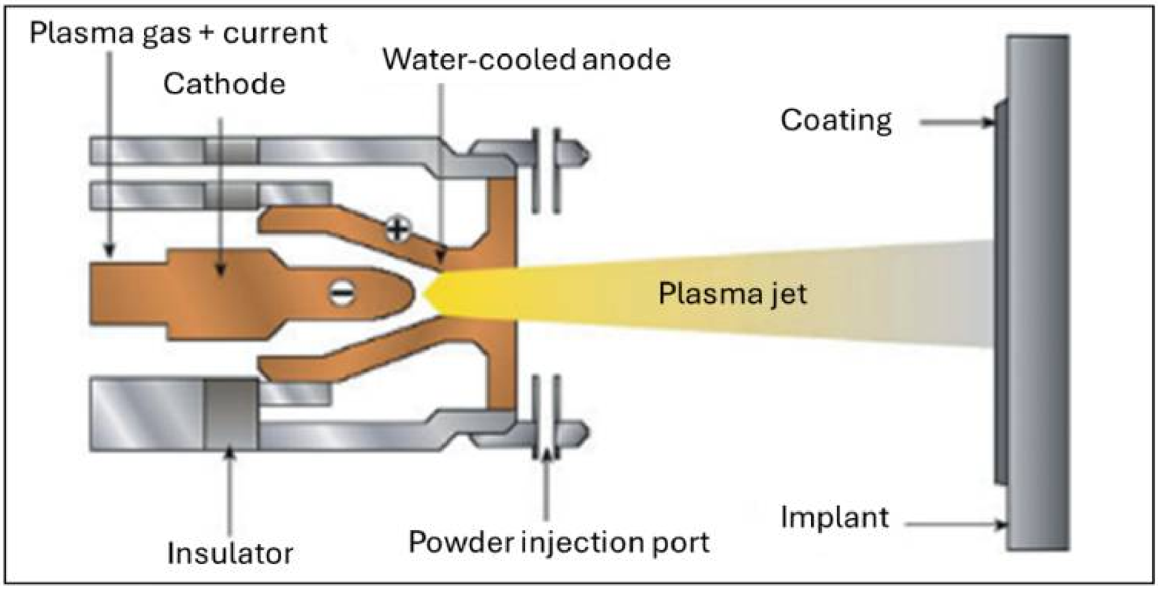

Figure 4. Schematic cross-section of an atmospheric plasmatron. © With permission of Walter de Gruyter GmbH, Berlin.

It is a versatile tool as any thermally reasonably stable metallic, ceramic, or even polymeric material with a well-defined congruent melting point can be coated onto nearly any surface. Frequently, some portion of the molten material rapidly quenched on contact with the relatively cool implant surface forms easily soluble amorphous phases such as ACP of variable composition as will be discussed below. Nevertheless, in practice many limitations persist related to coating thickness, porosity, thermal alteration, adhesion to the substrate, the presence of residual stresses, and line-of-sight restriction.

The physics of plasma spraying involves the action of a plasma originating from ionization in an electric potential field of a suitable gas, preferentially argon or nitrogen. A plasma is defined as the ‘fourth state of matter’, consisting of positively charged ions and electrons but also neutral gas atoms, and photons. Moving charges within the plasma column induce a magnetic field $\vec{B}$ perpendicular to the direction of the electric field with the current $\vec{j}$. The vector cross-product [$\vec{j}\times\vec{B}$] is the magnetohydrodynamic Lorentz force, the vector of which is mutually perpendicular to $\vec{j}$ and $\vec{B}$. Consequently, an inward moving force is created that constricts the plasma jet by the so-called magnetic or z-pinch. In addition to the magnetic pinch, there is a thermal pinch that originates from the decreasing conductivity of the plasma gas at the cooled inner wall of the anode nozzle, resulting in a current density increase at the center of the jet. Consequently, the charged plasma tends to concentrate along the central axis of the plasmatron, thereby confining the jet. As the result of these two constricting effects, the pressure in the plasma core increases drastically and the jet is blown out of the anode nozzle of the plasmatron with supersonic velocity [36].

5.3. Property Requirements and Performance Profile of Hydroxylapatite Coatings

The preferred deposition method of biomedical hydroxylapatite was and still is atmospheric plasma spraying (Figures 4, 5A,B). This is despite the fact that HAp suffers dehydroxylation and subsequent decomposition in the extremely hot plasma jet. Partially dehydroxylated HAp phases such as oxyhydroxylapatite (OHAp) or oxyapatite (OAp) are being restored to fully stoichiometric HAp in contact with extracellular fluid (ECF) *in vivo*. Nevertheless, despite its apparent drawbacks, to this date atmospheric plasma spraying is the only biomedical coating deposition method certified and approved by the US Food and Drug Administration (FDA) [38] and by many other national standardization authorities.

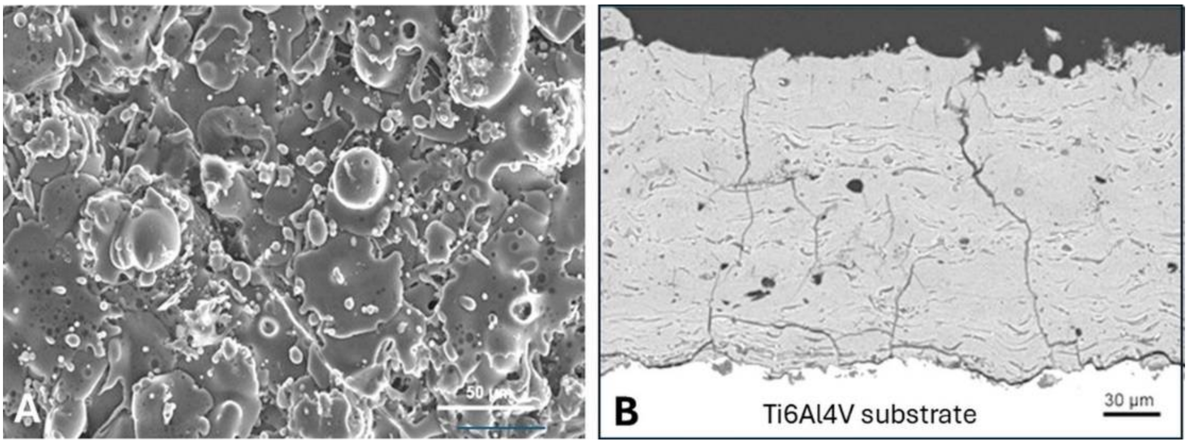

Figure 5. **A**: Typical surface morphology of a plasma-sprayed HAp coating with well-spread ‘pancake-like’ particle splats and some loosely adhering incompletely molten spherical particles. **B**: Cross-section of a thick plasma-sprayed HAp coating with all-through microcracks generated by tensile quenching stress. Coating thickness ~200 µm; average surface roughness 10 ± 0.5 µm; porosity 5 ± 1 vol%; tensile adhesion strength 50 ± 9 MPa [39,40]. © With permission by John Wiley & Sons.

One of the most crucial properties of HAp coatings is their biostability *in vivo* that increases with increasing (i) phase purity, (ii) crystallinity, (iii) coatings density, and (iv) coating thickness. As discussed below, requirements (i) and (ii) are poorly met by plasma spray technology owing to the incongruent melting behavior of HAp, and requirement (iii) must be relaxed to guarantee appropriate biological performance since a certain degree of porosity must be obtained for optimum cell in-growth. Finaly, requirement (iv) calls for a coating thickness of at least 50 µm. Although thicker coatings are more stable against *in vivo* resorption, they bear the risk of cracking, spalling, and delamination owing to increased residual coating stresses (Figure 5B; see also Section 5.3.8 below).

Coating integrity, cohesive and adhesion strengths, and surface roughness can be estimated by determining the flow characteristics of the molten particles using a simple ‘wipe’ test. A flat surface is quickly brought into the way of a molten particle trajectory with the intention to capture only a few particles. The solidified particle splats are being investigated with light optical or electron microscopy. Figure 6 shows typical examples of hydroxylapatite particle splats obtained from an argon/hydrogen plasma jet under low-pressure conditions [36]. The plasma enthalpy determined by the interaction of the plasma power and stand-off distance, increases from Figures 6A to 6D. In Figure 6A, the enthalpy supplied to the particle is insufficient to achieve melting. Figure 6B shows a splat pattern of a particle the outer rim of which has been melted, but its core has remained highly viscous as indicated by its porous microstructure. In Figure 6C, a well-molten splat is shown, whereas Figure 6D shows the somewhat exploded splat typical of a severely overheated particle.

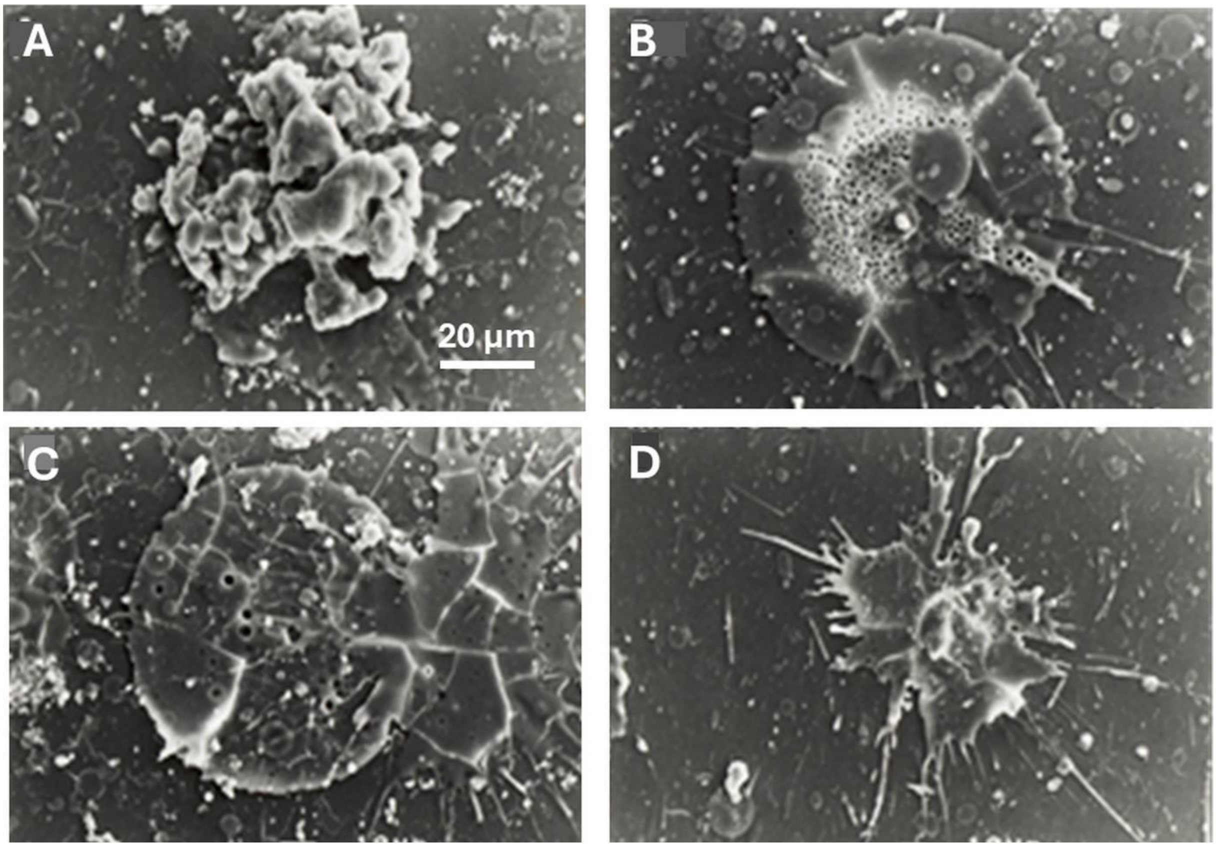

Figure 6. Hydroxylapatite particle splats produced by a 'wipe' test to determine the optimum settings of plasma power and stand-off distance. **A**: Plasma power 45 kW, stand-off distance 26 mm; **B**: Plasma power 30 kW, stand-off distance 24 mm; **C:** Plasma power 30 kW, stand-off distance 22 mm; **D**: Plasma power 45 kW, stand-off distance 22 mm [36]. © With permission of Wiley-VCH.

5.3.1. Incongruent Melting and Thermal Decomposition of HAp: Phase Composition

The temperature of the plasma jet of commercial APS equipment exceeds 15,000 K [36]. This extremely high temperature causes severe structural changes of HAp, even though the residence time of the powder particles in the plasma jet is very short, in the range of hundreds of microseconds to a few milliseconds. Since HAp melts incongruently at 1570°C (Figure 7A), it decomposes to tricalcium orthophosphate (α'-TCP, $Ca_3(PO_4)_2$), tetracalcium orthophosphate (TTCP, $Ca_4O(PO_4)_2$) and finally CaO during the four consecutive steps indicated in Table 1.

Table 1. Thermal decomposition sequence of hydroxylapatite [40].

Step 1:	$Ca_{10}(PO_4)_6(OH)_2$	→	$Ca_{10}(PO_4)_6(OH)_{2-x}O_x\square_x$ + xH_2O	Oxyhydroxylapatite (OHAp)
Step 2:	$Ca_{10}(PO_4)_6(OH)_{2-x}O_x\square_x$	→	$Ca_{10}(PO_4)_6O_x\square_x$ + $(1-x)H_2O$	Oxyapatite (OAp)
Step 3:	$Ca_{10}(PO_4)_6O_x\square_x$	→	2 $Ca_3(PO_4)_2$ + $Ca_4O(PO_4)_2$	TCP + TTCP (C_3P + C_4P)
Step 4a:	$Ca_3(PO_4)_2$	→	3 CaO + P_2O_5	Stepwise decomposition of TCP and TTCP
Step 4b:	$Ca_4O(PO_4)_2$	→	4 CaO + P_2O_5	

Based on this decomposition sequence, a simple shell model of the inflight evolution of calcium phosphate phases was adopted by Graßmann and Heimann [40], and Dyshlovenko et al. [41] (Figure 7B). Owing to the low thermal conductivity of HAp of ~1 W/mK, the inner core of a particle is still below the incongruent melting point and only dehydroxylation steps 1 and 2 come to bear, resulting in OHAp and OAp, short-range ordered (SRO) structures with lattice vacancies □. In contrast, the outer shells consist of a mixture of liquid TCP + TTCP (step 3) and liquid + solid CaO (step 4). According to Dyshlovenko et al. [41], there may exist a thin shell of solid TCP + TTCP. On impact with the cool surface of an implant to be coated, the outer liquid parts of the incoming particle splash and solidify preferentially as amorphous calcium phosphate (ACP).

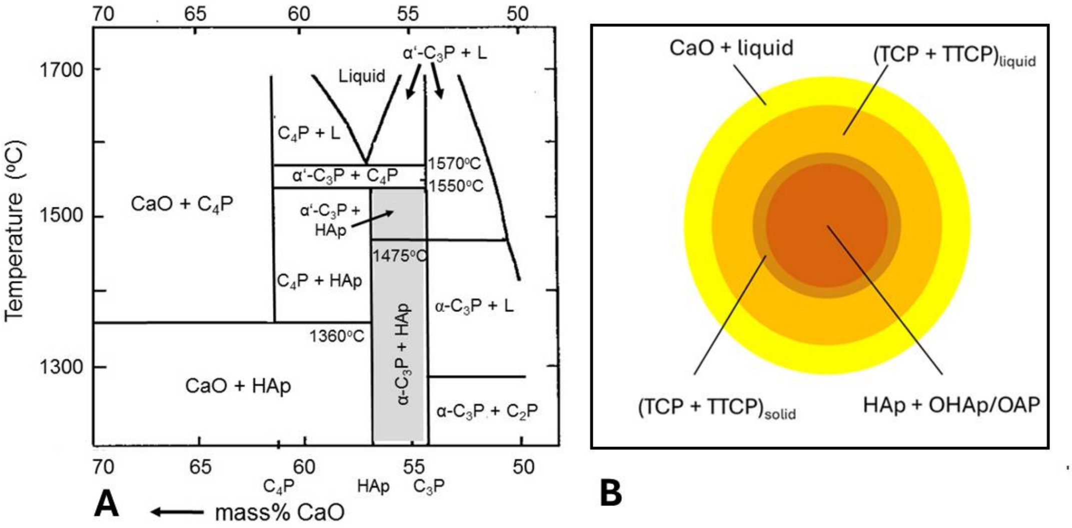

Figure 7. A: Partial quasi-ternary CaO-P$_2$O$_5$-(H$_2$O) phase diagram at a water partial pressure of 65.5 kPa (after Riboud [42]. The area of interest is shaded, showing the transformation of α-C$_3$P to α'-C$_3$P beyond 1475^{o}C and the incongruent melting of HAp and decomposition beyond 1570^{o}C to form C$_3$P (α'-TCP) and C$_4$P (TTCP). © With permission of Wiley-VCH. **B**: Schematic model of the thermal decomposition of a spherical HAp particle during flight in the high temperature plasma jet at a low water partial pressure of 1.3 kPa [41].

5.3.2. Degree of Crystallinity

As far as coating crystallinity is concerned, there are several aspects to consider. Fully crystalline and well-ordered HAp exhibits low solubility that does not lend itself easily to osseoconductivity as it causes the coating to behave largely like a bioinert material. Hence, fully crystalline, stoichiometric HAp has an inhibiting effect on cell proliferation owing to decreased alkaline phosphatase (ALP) activity [43]. The enzyme ALP is highly expressed in the cells of mineralized tissue and plays a critical function in the formation of hard tissue. Also, reduced osteocalcin secretion has been observed in the presence of fully crystallized and well-ordered hydroxylapatite [44]. Osteocalcin has routinely been used as a serum marker of osteoblastic bone formation and is believed to act in the bone matrix to regulate mineralization.

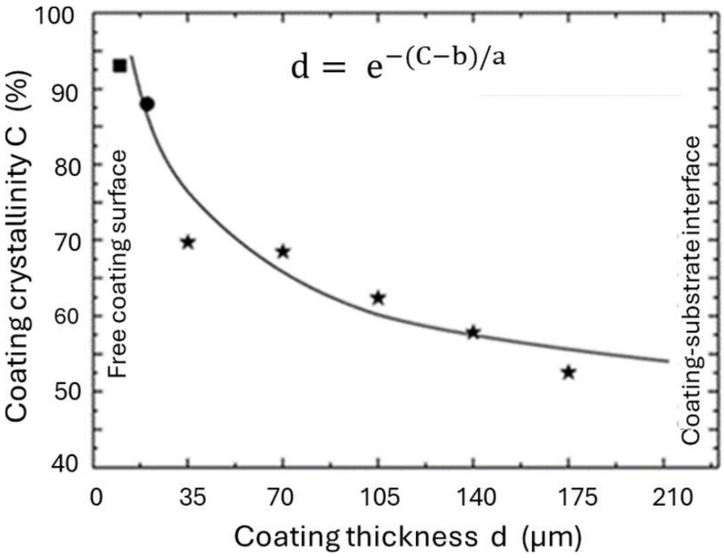

Preprints.org (www.preprints.org) | NOT PEER-REVIEWED | Posted: 23 May 2024 doi:10.20944/preprints202405.1476.v1

Figure 8. Exponential decrease of the crystallinity C of a plasma-sprayed HAp coating with increasing thickness d. The coefficients of the exponential decay equations were determined to be a = 128.3 and b = 14.3. Data were acquired by conventional X-ray diffraction (8 keV, square) and synchrotron radiation X-ray diffraction (11 keV, dot; 100 keV, stars) [45]. © With permission by Elsevier.

Synchrotron radiation X-ray diffraction of coating cross-sections reveals that the crystallinity of the coating decreases exponentially with depth, from about 93 % at the free surface to about 52 % at the coating-substrate interface (Figure 8). In parallel, the amount of more or less unchanged HAp decreases linearly from some 80 mass% (the remaining phases are 15 mass% TTCP, 4 mass% ß-TCP, and 1.5 mass% CaO) at the free coating surface to less than 15 mass% immediately at the metal interface [45]. Additional studies of the depth-resolved cross-sectional phase composition of plasma-sprayed HAp support this finding [46].

The amorphous calcium phosphate (ACP) (Figures 9A, B) accumulating at the immediate interface coating-substrate as the first product of solidification during plasma spaying provides a low energy-path of coating delamination [47] as it dissolves preferentially during *in vivo* exposure to extracellular fluid (ECF). A certain degree of resorbability/solubility is required to obtain a sufficiently high concentration of Ca^{2+} and PO_4^{3-} ions conducive to precipitating secondary HAp micro- to nanocrystals for sustained biomineralization and thus, osseointegration. Consequently, careful engineering of plasma spray parameters is mandatory. To control coating crystallinity, the application of a thin bond coat separating the metallic substrate and the HAp top coat has been suggested [48]. Advantages of titania, zirconia or zirconium titanate bond coats include [49]

- Increase of adhesion to both metal and HAp. For example, a titania bond coat is thought to act as an extension of the native oxide layer on metallic titanium that may interact with HAp to form a thin reaction layer of perovskitic calcium titanate.
- Reduction of thermal decomposition of HAp by inhibiting the heat flow due to the presence of a thin titania bond coat film with low thermal conductivity (~ 1 W/mK) as opposed to a Ti6Al4V substrate (~ 7 W/mK).
- Reduction of the formation of amorphous phase that forms by a quenching contact immediately at the metal interface. Increase of crystallinity is caused by the thermal barrier function of a bond coat that prolong solidification time and thus, allowing the ACP to nucleate apatite and to crystallize. Experimental NMR results [49] show that as-sprayed coatings without a bond coat contain only 46 mass% well-ordered HAp at the free coating surface as contrasted with 62 mass% in coatings with a titania bond coat. During incubation for 12 weeks in r-SBF [50], these values increase by dissolving TCP, TTCP, CaO, and ACP phases to 74 mass% and 92 mass%, respectively.
- Reduction of residual coating stresses by reducing the gradient of the coefficient of thermal expansion between the metal substrate and the ceramic overlayer.

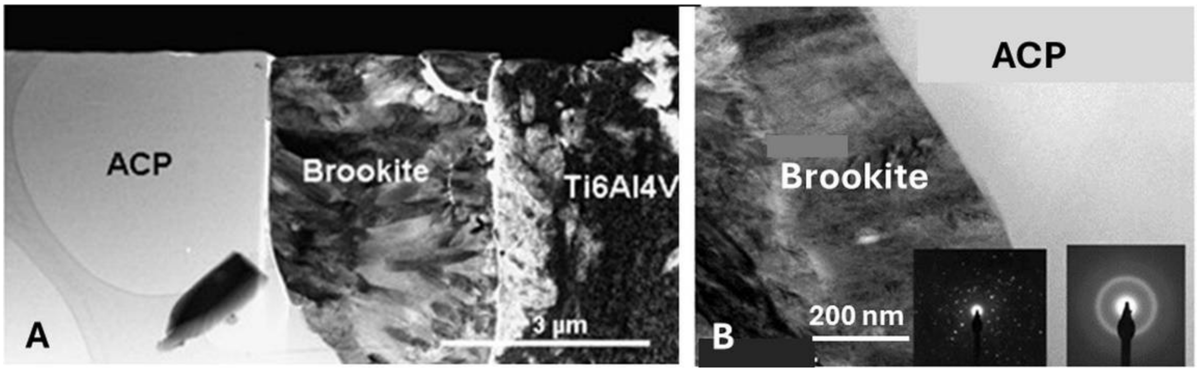

Figure 9. A: A scanning transmission electron microscopy (STEM) image of the cross-section of the interface between a Ti6Al4V substrate (right) and a plasma-sprayed titania (brookite) bond coat (center) and a calcium phosphate (ACP) layer (left). The sample was prepared by focused ion beam (FIB) cutting using Ga ions. **B:** Enlarged interface between columnar brookite crystals and ACP at

high magnification STEM. The insets show the electron diffraction pattern of both phases [37]. © With permission by Elsevier.

Figure 9A shows a STEM image of a cross-section of a plasma-sprayed titania bond coat separating the Ti6Al4V substrate from the innermost calcium phosphate layer consisting of ACP. As ascertained by Figure 9B, the bond coat was found to consist of the metastable orthorhombic brookite polymorph of titania with low surface energy instead of the expected rutile or Magnéli-type phases Ti_nO_{2n-1} and was likely formed as the result of quenching by a process akin to Oswald's rule of steps. The columnar brookite crystals interdigitate with both the ACP and the Ti6Al4V substrate and thus, provide strengthening of the mechanical performance by increased resistance against shearing forces *in vivo*.

5.3.3. Assessment of Structural Order in Hydroxylapatite Coatings: Raman and NMR Studies

Application of high temperature introduces severe structural disorder in as-received crystalline HAp that has noticeable repercussions on its mechanical, chemical, and biological behaviour. Detailed information on the structural order of calcium phosphate phases can be obtained by Raman and NMR spectroscopies [49,51–53]. Figure 10A shows the full range of the laser-Raman spectrum of an atmospheric plasma-sprayed HAp coating with the four principal vibration modes of the PO_4^{3-} tetrahedron indicated. Figure 10B shows the Gaussian-Lorentzian deconvolved principal Raman mode ν_1. The left shoulder at 949 cm^{-1} may be associated with ACP and the right shoulder at 971 cm^{-1} can be assigned to ß-TCP [54]. The splitting of the triply degenerate ν_3 and ν_4 modes shown in Figure 10A is presumably caused by an increasingly perturbed PO_4^{3-} environment owing to dehydroxylation and/or increased disorder of hydroxyl ions in the crystal lattice of HAp [51].

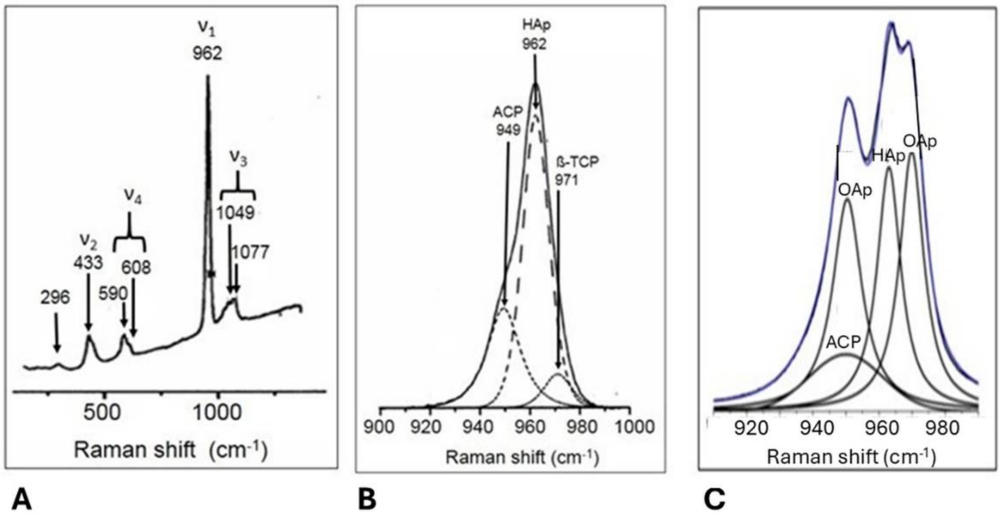

Figure 10. Laser-Raman spectra (λ = 514.6 nm; 5 mW) of plasma-sprayed HAp [54]. **A**: The four principal vibrational modes of the PO_4^{3-} tetrahedron: symmetric stretching mode of the P-O bond (ν_1), doubly degenerate O-P-O bending mode (ν_2), triply degenerate asymmetric P-O stretching mode (ν_3), and triply degenerate O-P-O bending mode (ν_4). **B**: Gaussian- Lorentzian deconvolution of the ν_1 vibrational mode into the contribution of well-ordered HAp [55] and those of the thermal decomposition product ß-TCP, and ACP [48,55]. © With permission by Wile-VCH. **C**: Gaussian-Lorentzian deconvolution of a low-energy plasma-sprayed (LEPS) HAp coating, showing distinct Raman bands of OAp [52]. © With permission by Elsevier.

Figure 9C reveals that during low-energy plasma spraying (LEPS) distinct high intensity bands of OAp are still present [52], in contrast to high-energy plasma spraying during which OAp decomposes to form ß-TCP and TTCP, consistent with step 3 of the decomposition sequence (Table 1). Consequently, when desired to maintain oxyapatite in the coating, the electrical energy input into the plasma spray process and thus, attainment of high temperature must be drastically reduced.

Even more detailed information on the degree of structural disorder that HAp suffers during plasma spraying has been obtained by high resolution X-ray diffraction [56] and solid-state nuclear magnetic resonance (NMR) spectroscopy [48,49,57,58]. Determining the position as well as the shift of ^{1}H-magic angle spinning (MAS) and ^{31}P-MAS NMR bands provide important clues to determine the environment of PO_4^{3-} tetrahedra and thus, allows identifying dehydroxylation phases such as OHAp and OAp as well as decomposition phases such as TCP and TTCP, as well as ACP.

Figure 11 shows the ^{1}H-MAS (A) and the ^{31}P-MAS (B) NMR spectra of a plasma-sprayed HAp coating [49,57,59]. The insets refer to completely ordered, stoichiometric, and highly crystalline HAp. In Figure 11A, the high intensity band L at -0.1 ± 0.1 ppm represents the proton band position of crystalline, stoichiometric HAp, and the isotropically shifted weak band L* at -1.3 ± 0.3 ppm may be assigned to protons present in OHAp. The broad M band at 5.2 ± 0,2 ppm indicates isolated pairs of strongly coupled protons in the channels parallel to the c-axis in HAp [57]. Band G at ~ 1.3 ppm may belong to free water molecules attached to the surface of HAp particles [58]. The ^{31}P-MAS NMR spectrum shown in Figure 11B is more complex. The principal band A at 2.3 ± 0.1 ppm is associated with highly crystalline hydroxylapatite (see inset) whereas the other bands of the Gaussian-Lorentzian deconvolved NMR spectrum represent dehydroxylation (B,C) and decomposition (D) phases. Band B at 1.5 ± 0.2 ppm signals a strongly distorted PO_4^{3-} environment without OH^- neighbours as suggested for OAp, and band C at 3.0 ± 0.2 ppm has been assigned to distorted PO_4^{3-} tetrahedra associated with single or paired OH^- ions as in OHAp [57]. Finally, band D at 5.0 ± 0.2 ppm may represent very strongly distorted PO_4^{3-} tetrahedra bare of OH^- ions as present in TCP, TTCP, and OAp.

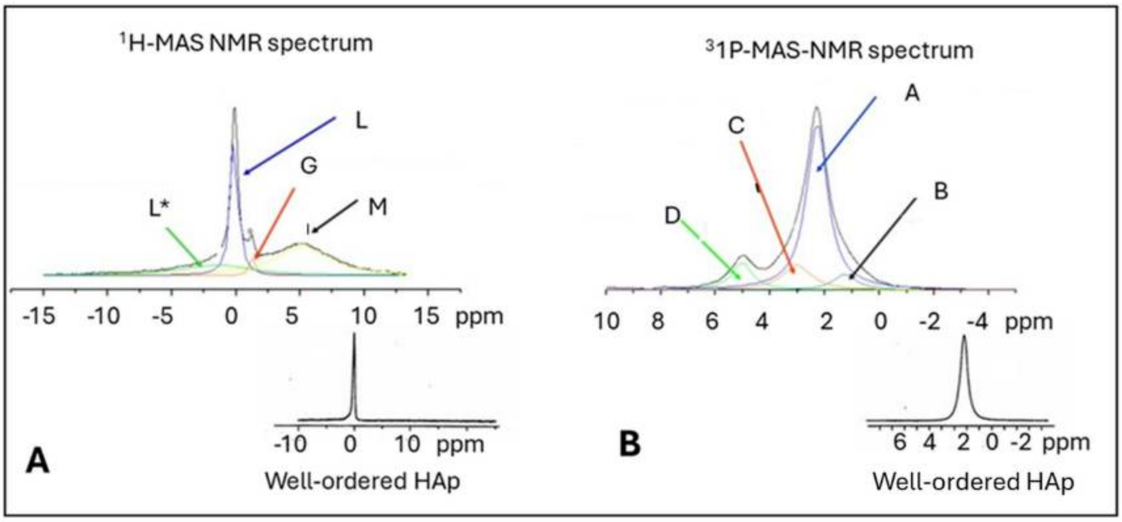

Figure 11. ^{1}H-MAS (**A**) and the ^{31}P-MAS (**B**) NMR spectra of a plasma-sprayed HAp coating. For assignment of spectral bands see text. © Image courtesy Dr. Thi Hong Van Tran [59].

Supporting 2D-double quantum ^{1}H/^{31}P cross-polarization (CP) heteronuclear correlation (HETCOR) NMR spectroscopy (Figure 12) further suggests that the D-band may indeed represent OAp, the chemical shift of which is identical to that of TCP and TTCP, thus, confirming the thermal decomposition sequence HAp → OHAp → OAp → TTCP/TCP shown in Table 1.

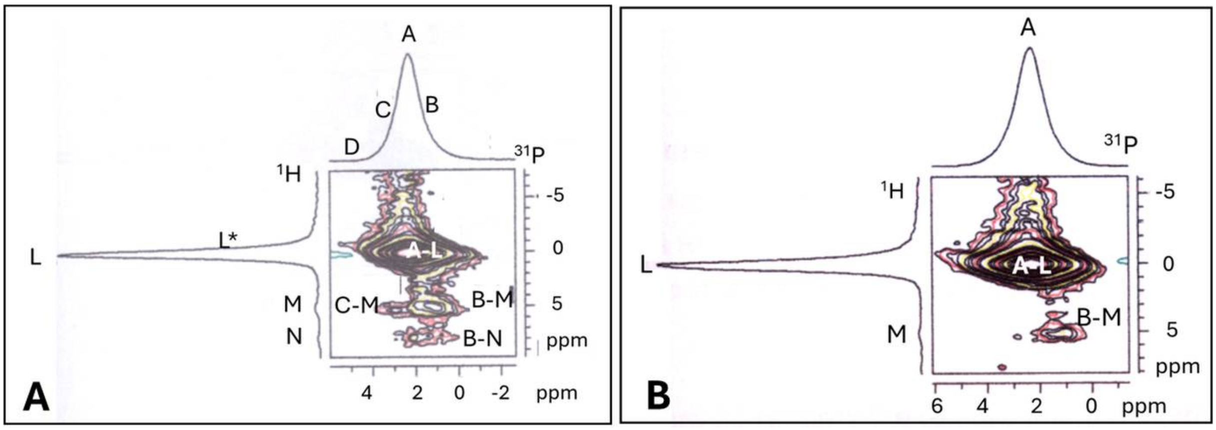

Figure 12. 2D-^{1}H/^{31}P-CP-HETCOR NMR spectra of a plasma-sprayed HAp coatings. **A**: As-plasma-sprayed **B**: Incubated in r-SBF [50] for 8 weeks. © Image courtesy Dr. Thi Hong Van Tran [59].

Figure 12A shows the main A-L correlation band of crystalline, stoichiometric HAp together with the weak satellite correlation bands C-M and B-M that can be associated with a partially dehydroxylated apatite structure, *i.e.* OHAp *sensu lato* and Ca-deficient ACP, respectively [48]. The correlation bands B-L and C-L are swamped by the intense A-L band but can be visualized by Gaussian-Lorentzian deconvolution of the A-L band (not shown). The weak and broad band N in the individual proton spectrum at ~ 7.5 ppm was assigned to isolated OH-groups in the c-channel of HAp [60]. Figure 12B shows the same coating incubated in r-SBF [50] for 8 weeks at 37 ± 0.5°C. The satellite correlation bands C-M and B-N have disappeared and B-M has weakened, indicating that SRO phases were dissolved. In parallel, the intensity of the A-L band of more or less pure, stoichiometric hydroxylapatite has increased, reflecting its relative increase from about 67 mass% in the as-sprayed coating to 85 mass% after 8 weeks of incubation. In parallel, the amount of TTCP decreased from about 26 mass% to 10 mass%, whereas that of ß-TCR remained nearly constant at 5 mass%. Minor amounts of CaO around 1.5 mass% have disappeared completely after a few days of incubation [59].

In addition, quantitative ^{31}P magic angle spinning (MAS) solid-state NMR allows distinguishing between PO_4^{3-} groups of apatitic calcium phosphates and HPO_4^{2-} groups of non-apatitic calcium phosphates (Figure 13). Non-apatitic calcium phosphate is thought to be a measure of the maturity of bone whereby with time, the non-apatitic precursor transforms to true apatite [61].

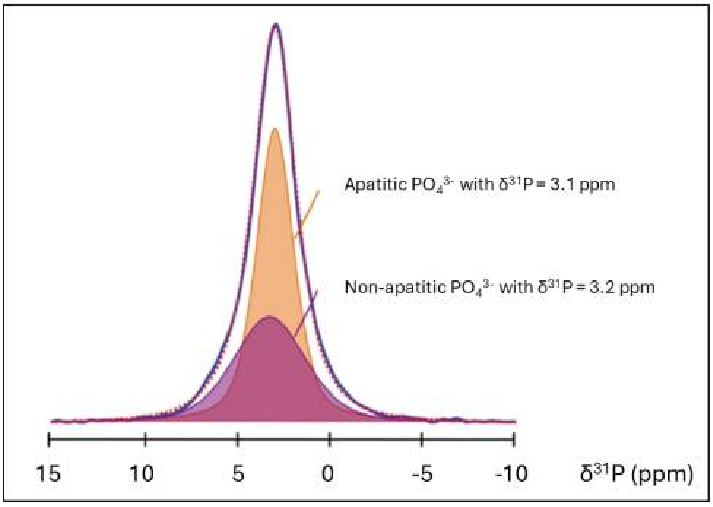

Figure 13. Solid-state ^{3}1P NMR-MAS spectrum of bone of a 2 year-old sheep (blue envelope) and its deconvolution into a well-ordered and stoichiometric apatitic core (orange) and a HPO_4^{3-}-containing amorphous non-apatitic calcium phosphate surface layer (purple) [62]. © Permission granted under Creative Commons Attribution 4.0 International License.

For a long time, biological apatite has been described as Ca- and OH-deficient carbonated hydroxyapatite (CHA) in which a fraction of the PO_4^{3-} lattice sites is occupied by HPO_4^{2-} ions, resulting in the approximate formula of $Ca_{10-x}(HPO_4)_x(PO_4)_{6-x}(OH, O, Cl, F, CO_3, \square)_{2-x} \cdot nH_2O$; $0 < x < 1$; n = 0-2.5 (see above). However, more recent solid-state NMR studies have revealed that the surface of mature bone mineral particles does not consist of well-ordered HAp at all but of hydrated ACP [62], a contention that mirrors an earlier suggestion by Jäger et al. [58] who proposed that HAp nanoparticles consist of a well-ordered, stoichiometric, and highly crystalline core covered by an extremely thin (~ 1nm) layer of disordered calcium phosphate with a Ca/P-ratio of ~ 1.5.

5.3.4. Crystallographic Structure of Hydroxylapatite

Figure 14A shows the crystallographic structure of hydroxylapatite in a ball-and-spoke model. Hydroxylapatite (HAp), $Ca_{10}(PO_4)_6(OH)_2$ is a member of a large group of chemically different but structurally identical compounds of space group $P6_3/m$, and with the general formula $\mathbf{M}_{10}(\mathbf{Z}O_4)_6\mathbf{X}_2$ (**M** = **Ca**, Pb, Cd, Zn, Sr, La, Ce, K, Na; **Z** = **P**, V, As, Cr, Si, C, Al, S; **X** = **OH**, Cl, F, CO_3, H_2O, ☐). In stoichiometric HAp, Ca polyhedra share faces to form chains parallel to the crystallographic c-axis [00.1] that constitutes a 6_3 screw axis. These chains are linked into a hexagonal array by sharing edges and corners with PO_4 tetrahedra. The OH^- ions are located in wide hexagonal channels parallel [00.1].

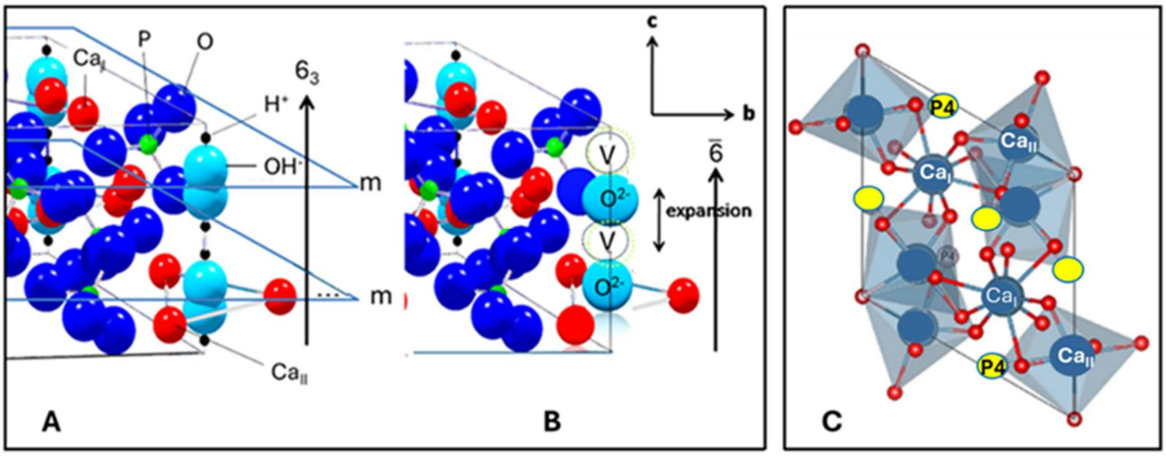

Figure 14. A: Ball-and-spoke model of the unit cell of HAp (space group $P6_3/m$). Mirror planes m are at z = ¼ and ¾, perpendicular to the 6_3 screw axis [63]. **B**: Hypothetical structure of OAp (space group $P\bar{6}$) with a chain of O^{2-} ions separated by vacancies V parallel to [00.1] [19,64] © With permission by Wiley-VCH. **C:** The Ca atoms (blue grey) are arranged in two crystallographic positions: Ca_I coordinated by nine oxygen atoms (red) at z = 0 and ½ along the threefold a_i axes, and Ca_{II} atoms irregularly coordinated with six oxygen atoms and five orthophosphate groups at z = ¼ and ¾. PO_4^{3-} tetraeder positions (P4) are shown in yellow. © Permission granted under Creative Commons Attribution 4.0 International License.

Owing to its open channel structure, HAp can incorporate a wide range of other ions that substitute either Ca^{2+} cations or OH^- and PO_4^{3-} anions. This happens without large distortion of the crystal lattice, thus maintaining the $P6_3/m$ space group of pure stoichiometric HAp. In biological apatite, Ca^{2+} is being partially substituted by metabolically important cations such as Na^+, Mg^{2+}, Sr^{2+}, K^+ and some trace elements such as Pb^{2+}, Ba^{2+}, Zn^{2+} and Fe^{2+}. Replacement of PO_4^{3-} with CO_3^{2-}, SiO_4^{4-} and SO_4^{2-} anions as well as OH^- with Cl^-, F^- and CO_3^{2-} contributes to a host of biochemical pathways in which bone matter is involved. [27,65,66]. It is this compositional variability of biological apatite that is the root cause of its high biocompatibility and osseoconductivity. In particular, the OH^- positions can be occupied by mobile O^{2-} ions and lattice vacancies and thus, assist in the kinetics of dehydroxylation of HAp during plasma spraying and biomineralization *in vivo*.

5.3.5. Oxyapatite: Fact or Fiction?

Oxyapatite (OAp), $Ca_{10}O(PO_4)_6$ is thought to be the product of complete dehydroxylation of HAp [12] but converts back to stoichiometric HAp in the presence of water either during cooling of the as-sprayed coating in moist air or by *in vivo* reaction with extracellular fluid (ECF). As discussed in Section 3 above, there is evidence against the existence of OAp as a thermodynamically stable phase.

According to past investigations into the structure of OAp, there may exist a linear chain of O^{2-} ions parallel to the c_0-axis, each one followed by a vacancy [19] (Figure 14B). Calculations by density-functional theory with local-density approximation (DFT-LDA) and first-principles pseudo-potentials [20] suggested a hexagonal 'c-empty' structure $Ca_{10}(PO_4)_6\square_2$ with a stable total-energy minimum. During thermal dehydroxylation, the mirror planes m (Figure 14A) of the parent HAp are lost, thereby transforming the symmetry of the screw axis 6_3 to that of the polar axis $\overline{6}$.

The detection of OAp by conventional X-ray diffraction is difficult if not impossible since the c_0-axis length of OAp is only marginally larger than that of HAp [67]. This accounts for only a small shift of the (00.2) interplanar spacing toward smaller diffraction angles. Consequently, very accurate measurements are required using, for example, X-ray diffraction by synchrotron radiation or neutron diffraction techniques. Indeed, high resolution synchrotron X-ray diffraction (Figure 15) reveals that the average c_0 distance of OAp is with 0.6900 nm about 0.3% longer than the c_0 lattice distance of stoichiometric HAp (0.688 nm), confirming the postulated expansion of the unit cell that is presumably caused by the larger Shannon radius of the O^{2-} ion (135 pm) compared to that of the OH^- ion (118 pm) [64].

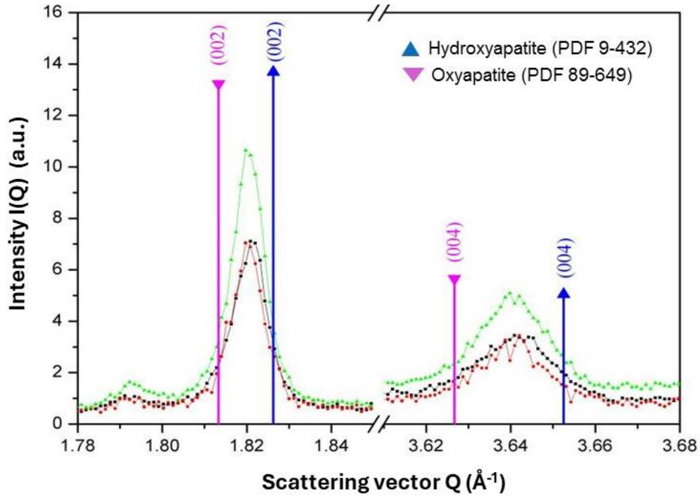

Figure 15. Scattering vectors $Q = 4\pi \cdot \sin \Theta/\lambda$ of synchrotron X-ray diffraction profiles of the (00.2) and (00.4) interplanar spacings of three plasma-sprayed HAp coatings [22]. © With permission by Wiley-VCH.

5.3.6. Transformation of Amorphous Calcium Phosphate (ACP)

Of the sixteen available positions for OH^- ions in the unit cell of HAp, only 50% are statistically occupied, leaving 8 vacancies along [00.1]. This leads to direction-dependent differences in the mobility of OH^- ions as well as the associated Ca^{2+} ions, relevant for the transformation of ACP to crystalline HAp, either *in vitro* in contact with simulated body fluid (SBF) (Figure 16) or *in vivo* by extracellular fluid (ECF) contact. The extent of electrical conductivity [68] as well the kinetics of the stepwise dehydroxylation forming OAp [22] is also dependent on the mobility of OH^- ions.

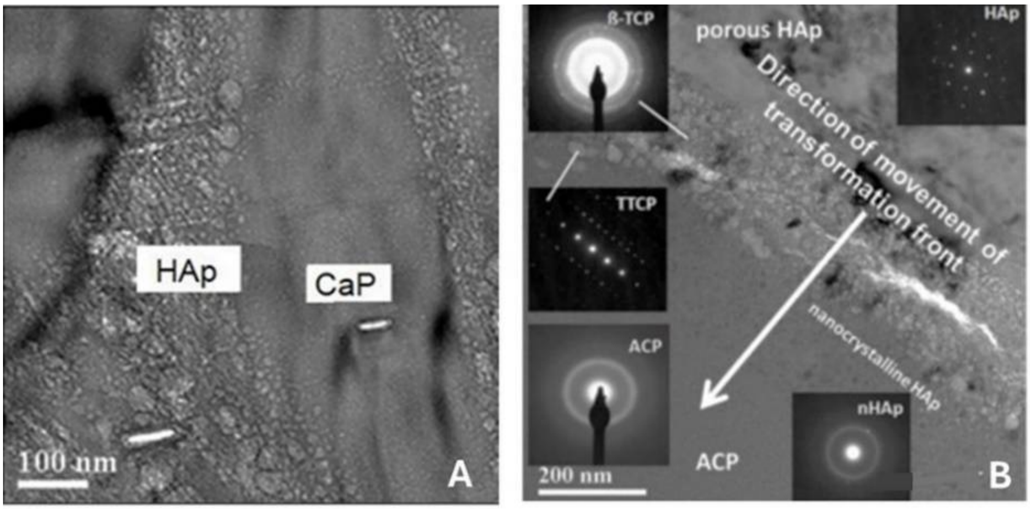

Figure 16. A: Porous crystalline HAp with Ca/P = 1.65 formed by transformation of amorphous CaP with Ca/P = 1.36 on contact with r-SBF for 24 weeks [69]. © With permission by Elsevier. **B:** STEM image of the transformation of ACP to crystalline CaP phases on contact with r-SFB for 1 week. The insets show electron diffraction pattern of ACP with a single diffuse ring at d = 0.809 nm corresponding to {10.0} of HAp (bottom left), well-crystallized HAp (upper right), nanocrystalline HAp with two diffuse rings at d = 0.288 assigned to {21.0/21.1} and 0.251 nm assigned to {30.1} (bottom right), and ß-TCP and TTCP (left) [48]. © With permission by Wiley-VCH.

Figure 16A shows the formation of porous crystalline HAp from ACP during *in vitro* contact with r-SBF [69]. Crystallization likely occurs by fluid flow of SBF along cracks and fissures within the coating (Figure 16B) to form porous HAp with Ca/P = 1.65 as well as dense, needle-like crystalline Ca-depleted calcium orthophosphate CaP with Ca/P ~ 1.36. Such needles with comparable composition thought to be akin to bone-like apatite can nucleate from ACP and are implicated with mediating osseointegration [70].

The scanning transmission electron microscope (STEM) image of Figure 16B demonstrates how during incubation of the coating in r-SBF the transformation front sweeping across the coating layer changes ACP to crystalline phases. At the trailing edge of the transformation front, porous well-crystallized HAp is formed (upper right corner), whereas at the leading edge nanocrystalline HAp appears. In addition, within the transformed section of ACP, ß-TCP and TTCP crystallites were detected [48].

5.3.7. Coating Porosity, Surface Roughness, and Surface Nanotopography

Coating porosity and surface roughness play decisive roles in the quest for enhancing the biomedical performance of endoprosthetic implants. On the one hand, optimum coating porosity, pore size distribution, and fractal surface roughness are preconditions for uninhibited ingrowth of bone cells [71]. On the other hand, the denser the coating, the lower is the risk of bonding degradation by cracking, spalling, delamination, or dissolution during *in vivo* contact with aggressive ECF [72]. These two conflicting requirements of the need of sufficient porosity for anchoring bone cells, and the need of high coating density for superior adhesion to the substrate have to be carefully considered, balanced, and controlled [40]. This is particularly important in view of the risk of release of coating particles that will be distributed by the lymphatic system throughout the body and is known to lead to inflammatory responses with formation of giant cells and phagocytes [73]. Hence, balancing the two conflicting porosity requirements is a considerable challenge during designing and controlling appropriate intrinsic plasma spraying parameters. Parameters controlling coating porosity include powder particle size and the degree of particle melting that in turn is a complex function of plasma gas composition, plasma enthalpy, powder injection geometry, and spray distance [36]. This type of porosity control is difficult since plasma spraying results frequently in rather dense coating layers unable to satisfy biomedical needs that stipulates pore sizes of at least 75 µm [74]. Figure 17 shows the effect of the degree of particle melting, expressed as fraction of molten particles, on porosity, crystallinity, and adhesive bond strength of plasma-sprayed HAp [75].

doi:10.20944/preprints202405.1476.v1

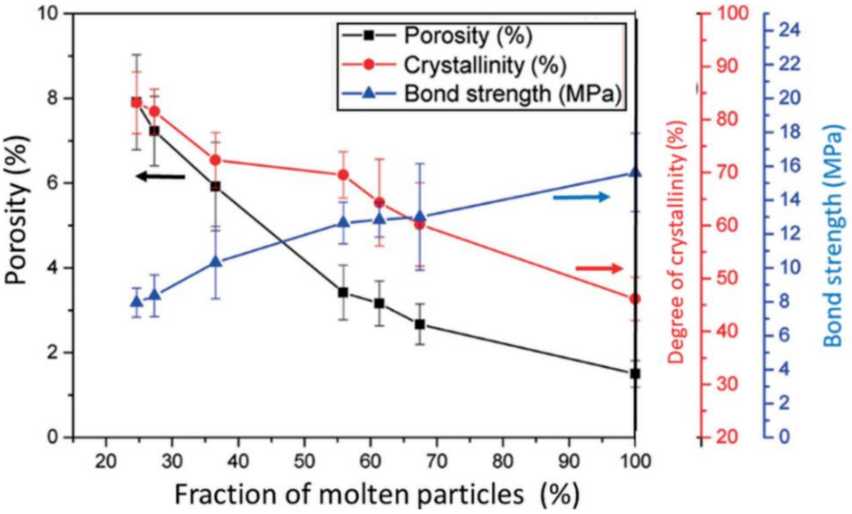

Figure 17. Dependence of porosity (left), degree of crystallinity and bond strength (right) of plasma-sprayed hydroxylapatite coatings on the degree of particle melting [75]. © With permission by Elsevier.

Optimum surface nanotopography is an important prerequisite for optimum cell adhesion and proliferation. To define the general nature of micro- and nano-roughened plasma-sprayed surfaces, fractality theory has been invoked [76,77]. Using a fractal approach, Gentile et al. [78] conducted experiments to study cell proliferation on electrochemically etched silicon proxy surfaces with varying roughness but comparable surface energies. The surface profiles were found to be self-affine fractals, the average roughness *R*a of which increased with increasing etching time from ~2 nm to 100 nm, with fractal dimension ranging from $D = 2$ (a nominal flat surface) to $D = 2.6$. Moderately rough surfaces with *R*a between 10 and 45 nm yield a close to Brownian surface topography with $D \sim 2.5$. The observed cell behavior was linked to the theory of adhesion to randomly rough solids. A moderately rough surface with large fractal dimension supports efficient cell proliferation. Gittens et al. [79] critically reviewed and interpreted the influence of surface topography including microroughness and nanostructures on the osseointegration of spinal implants. They found that next to the implant design, the experience of the physician and patient variables, the success of spinal implants is largely dependent on the surface characteristics of the device, including surface roughness, surface chemistry, and surface energy. This has been echoed by a recent review on the role of implant surface modification in osseointegration [80]-

5.3.8. Residual Coating Stresses

Plasma spraying is a rapid solidification process during which the molten or semimolten particles strike the substrate surface with supersonic velocity that may even lead to reverberating shock waves that provide additional heat to the deposit and slow down its solidification by a thermal pressure component [36,81]. Determination of the direction and the extent of residual coating stresses can be experimentally assessed by X-ray diffraction ($\sin^2\Psi$-technique), Almen-type curvature measurements, hole-drilling strain gauge method, or photoluminescence and Raman piezospectroscopies [8].

Control of residual coating stresses is mandatory to obtain HAp deposits that adhere well to the implant substrate and thus, guarantee reasonable resistance to chipping, spalling, and complete delamination. The large temperature gradient experienced during the plasma spray process generates residual stresses in the deposited coating [36]. There are two main types of stress, thermal and quenching stress that combined with the complicated solidification process within the coating, are the two main contributors to the overall residual stress [27].

The principal equation governing the generation of *thermal stress*, σ_c has been derived by the German glass chemist Adolf H. Dietzel and can be expressed by the equation

$$\sigma_c = \{E_c(\alpha_c - \alpha_s)\frac{\Delta T}{1-\nu_c} + [\frac{1-\nu_s}{E_s}](\frac{d_c}{d_s})\} \qquad (1)$$

where E is the modulus of elasticity, α is the coefficient of thermal expansion, ΔT is the temperature difference between coating and substrate, ν is the Poisson's number, and d is the thickness. The subscripts c and s refer to coating and substrate, respectively. Since at given values of E and ν the thermal coating stress σ_c increases with increasing coating thickness d_c, the risk of spalling is much higher in thick coatings than in thin ones. Moreover, depending on the sign of (α_c–α_s), the thermal stress can either be tensile or compressive.

The origin of *quenching stress* lies in the effect of molten particles impacting the cool substrate whereby their contraction during solidification is restricted by clamping adherence to the roughened substrate surface. This leads to tensile stress in the coating [82–86], frequently resulting in cracking when the cohesive coating strength can be overcome (Figure 5B). The first layer adjacent to the interface, found to consist of ACP [69], will crucially control the occurrence of residual stresses in terms of their magnitude as well as their signs. This thin ACP layer provides a low-energy fracture path that may lead to coating delamination in the post-operative presence of tensile or shear stresses *in vivo*. The transformation of ACP (Figure 16) to crystalline calcium phosphate phases during *in vitro* contact with SBF [69,87] and presumably *in vivo* contact with ECF, respectively, will result in stress relaxation [88], thus, reducing the risk of coating failure by delamination. Figure 18A shows the strain $\varepsilon = (d–d_0)/d_0 \cdot 10^{-3}$ of as-sprayed and incubated HAp coatings deposited by atmospheric plasma spraying on Ti6Al4V substrates as a function of $\sin^2\psi$, where ψ is the tilt angle toward the X-ray beam [89,90].

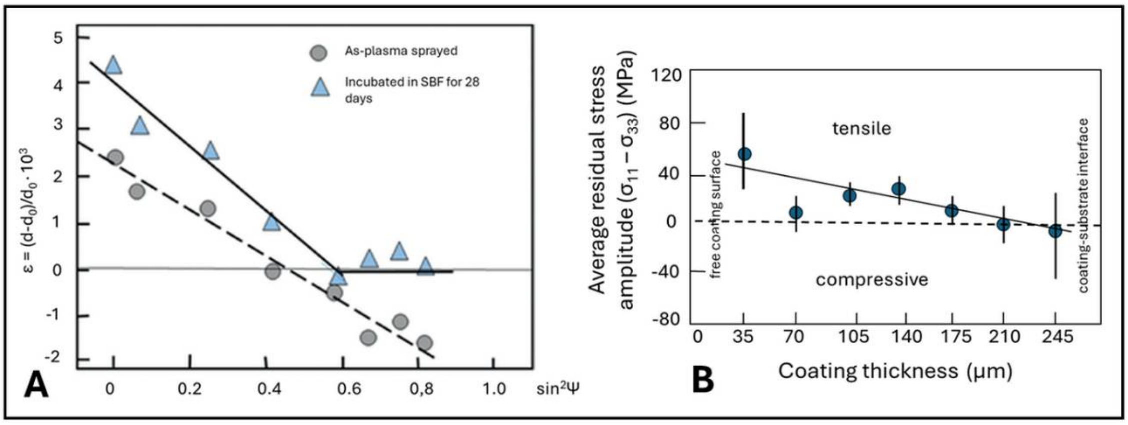

Figure 18. **A**: Strain ε of an as-plasma sprayed HAp coating (dots) and coatings incubated for 28 days in r-SBF [50] (triangles) [89,90]. **B:** Residual stress amplitude (σ_{11}-σ_{33}) of a plasma-sprayed HAp coating showing that close to the coating-substrate interface the residual tensile stress amplitude changes sign and becomes weakly compressive [45]. © With permission by Elsevier.

When the coating is in tension, $\varepsilon \propto d\text{-}d_0$ increases, when in compression it decreases. As shown in Figure 18A, the plasma-sprayed HAp coatings measured by the $\sin^2\Psi$ method is at a rather strong tensile stress owing to thermal mismatch developed during cooling of the deposited layer to room temperature. This tensile stress will relax during incubation in SBF when high levels of ACP thought to be a main contributor to the residual stress transforms to different calcium phosphate phases (see Figure 16B), most notably TTCP and Ca-depleted defect HAp. Hence, the layer of bone-like secondary apatite deposited at the outermost rim of the samples will be decoupled from the declining stress field, and thus, shows close to zero stress (triangles in Figure 18A). At the free coating surface, the tilt angle Ψ is 0° ($\sin^2\Psi = 0$), *i.e.* the X-ray beam is tangential to the surface in grazing incidence. With increasing tilt angle Ψ, deeper areas of the coating are being probed until at 90° ($\sin^2\Psi = 1$) the coating-substrate interface is being reached by the probing X-ray beam, and the character of the stress changes from tensile to slightly compressive.

Residual stress analyses using synchrotron radiation (11 and 100 keV) X-ray diffraction allow more detailed insight into the mechanisms of stress development and relaxation [45]. The principal

Cauchy stress tensor components σ_{11} and σ_{33} are both tensile adjacent to the coating–substrate interface but relax to zero within the first 80 µm of the coating. With further accumulating coating thickness, the component σ_{11} slightly increases to become tensile again with +20 MPa at the free coating surface. In contrast, the tensile stress component σ_{33} at the coating–substrate interface decreases monotonously to compressive with −30 MPa at the free coating surface. This interplay of the two tensor components causes the average residual stress amplitude (σ_{11}-σ_{33}) to become quasi-linear as shown in Figure 18B.

5.3.9. Adhesion of Plasma-Sprayed Hydroxylapatite Coatings

The mechanical performance of plasma-sprayed hydroxylapatite coatings is largely determined by the quality of their adhesion to the metallic implant surface, whereby the degree of adhesion between coating and bone can be determined from retrieved orthopaedic implants [91,92]. From these studies it became apparent that the clinical success of HAp-coated implants is not only the result of sufficient adhesion of the coating to the implant surface, but in addition depends on many other non-material variables, including the skill of the surgeon to properly place the implant at the correct angle, the health and quantity of the cortical bone bed, and the age and physical condition of the patient.

The adhesion of plasma-sprayed hydroxylapatite layers to the implant surface was found to be notoriously weak. This is frequently in contrast to the desired rather high value in excess of 35 MPa [74]. In recognition of this problem, the ISO 13779-2 norm relaxed this value to at least 15 MPa [93]. For a long time, it was generally assumed that the sole contributor to adhesion of plasma-sprayed coatings is mechanical interlocking of the solidified particle splats with asperities of the roughened substrate surface. However, in a modern view, chemisorption and epitaxial/topotaxial processes are considered important alternative mechanisms contributing to coating adhesion [94,95]. There are claims that thin reaction layers of calcium dititanate ($CaTi_2O_5$) or calcium titanate (perovskite, $CaTiO_3$) may exist that mediate adhesion [96,97]. The control of apatite nucleation by calcium titanate surfaces has been explained by an epitaxial structural relationship between the (022) lattice plane of calcium titanate and the (00.1) lattice plane of hydroxylapatite [98]. However, the visualization of reaction layers by transmission electron microscopy even at very high magnification is counteracted by their intrinsic tenuity, since the very short diffusion path lengths of Ca^{2+} and Ti^{4+} ions, respectively render any potential reaction zone extremely thin.

Given these constraints, the jury is still out on the efficacy of adhesion-mediating reaction layers. To achieve higher adhesion strength, the degree of melting and superheating, respectively, of the HA particles in the plasma jet could be enhanced by an increase of the plasma enthalpy. However, there is an obvious conflict. High plasma enthalpy inevitably leads to increased thermal decomposition of hydroxylapatite and thus, to a decrease of its resorption resistance and in turn affects the *in vivo* longevity of the coatings. Consequently, the plasma spray parameters and the resulting microstructure of the deposited coatings need to be carefully optimized by controlling the heat transfer from the hot core of the plasma jet to the center of the powder particles.

6. Concluding Remarks

At present, total hip arthroplasty (THA) is among the most frequently performed and in their long-term outcome most successful and effective surgeries worldwide. Application of atmospheric plasma-sprayed (APS) osseoconductive hydroxylapatite (HAp) coatings to the metallic stem and the casing of the acetabular cup of hip endoprostheses assists in the in-growth of bone cells. The HAp coating prevents an acellular connective tissue capsule forming around the implant as a response to the introduced foreign body. The HAp layer will support bonding osteogenesis that through ‘bony in-growth’ allows transmitting the tensile and shear forces acting on the hip joint during locomotion. Clinical evidence has overwhelmingly confirmed that a long-term stable osseoconductive HAp coating will elicit a specific biological response at the interface of the implant material by controlling its surface chemistry through adsorption of bone growth-mediating factors. These factors include platelet-derived growth factor (PDGF) AA, insulin-like growth factors (IGFs) I and II, cytokines such as interleukin-6, colony-stimulating factors, and tumor necrosis factor-α, as well as non-collagenous matrix proteins such as osteocalcin, osteonectin, silylated glycoproteins, and proteoglycans. Their action will result in the eventual establishment of a strong and lasting bond between living tissue and biomaterial by osseointegration.

Even though deposition of hydroxylapatite coatings by atmospheric plasma spraying (APS) comes across as a mature and well research-supported process, there is a growing need to address several shortcomings. Exposure of HAp to the extreme temperature of the plasma jet during plasma spraying leads to dehydroxylation, forming oxyhydroxylapatite and/or oxyapatite as well as to partial or even complete thermal decomposition to tri- and tetracalcium orthophosphates as well as amorphous calcium phosphate (ACP), owing to incongruent melting of HAp. The large temperature gradient between the cool substrate and the superheated molten particle droplets, and the solidification kinetics after deposition generate residual coating stresses that are the root cause of formation of coating cracks and may lead to post-implantation delamination *in vivo*. Finally, line-of-sight limitation during the plasma spray deposition process prevents complex-shaped implant structures to be effectively coated by hydroxylapatite.

Consequently, owing to the complexity of the interaction among numerous plasma spray parameters that influence key coating properties, during the past decades many attempts have been made to optimize essential properties of osseoconductive hydroxylapatite coatings. These properties include coating thickness, phase composition, crystallinity, porosity, micro- and nano-roughness of coating surfaces, coating adhesion and cohesion, and residual coating stresses. In particular, maintenance of phase composition at values imposed by national and international norms [27,93], and controlling coating porosity by implementing novel deposition techniques such as suspension (SPS) or solution precursor plasma spraying (SPPS) are high up on the agenda of current research worldwide. In addition, research is progressing beyond hydroxylapatite coatings, aimed to design and develop novel intelligent coatings [99] responsive to changes in pH, temperature, light, piezoelectric, and magnetic stimuli that may provide osseoimmunomodulation and angiogenesis that in turn, promote osseogenesis and reduce inflammatory responses via foreign body reaction (FBR).

References

1. Merfort, R., Maffulli, N., Hofmann, U.K. et al. (2023). Head, acetabular liner composition, and rate of revision and wear in total hip arthroplasty: a Bayesian network meta-analysis. *Sci Rep* **13**, 2032. https://doi.org/10.1038/s41598-023-47670-
2. Heimann, R.B., Schürmann, N., Müller, R.T. (2004). *In vitro* and *in vivo* performance of Ti6Al4V implants with plasma-sprayed osteoconductive hydroxylapatite-bioinert titania bond coat 'duplex' systems: An experimental study in sheep. J. Mater. Sci. Mater. Med., 15(9), 1045-1052.
3. Hegde, V., Stambough, J.B., Levine, B.R., Springer, B.D. (2023). Highlights of the American Joint Replacement Registry Annual Report. Arthroplast. Today, 21: 101137.
4. Grimberg, A., Lützner, J., Melsheimer, O., Morlock, M., Steinbrück, A. (2023). EPDR Annual Report 2023. EPDR Deutsche Endoprothesenregister gGmbH, Berlin. https://www.epdr.de/fileadmin/...
5. Global Hip Replacement Implants Market Report and Forecast 2023-2031. https://www.researchandmarkets.com/reports/5797997.
6. Itiravivong, P., Promasa, A., Laiprasert, T., Techapongworachai, T., Kuptnitazsaikul, S., Thanakit, V., Heimann, R.B. (2003). Comparison of tissue reaction and osteointegration of metal implants between hydroxyapatite/Ti alloy coat: An animal experimental study. J. Medical Assoc. Thailand, 86(2), S422-S430.
7. Zhang, D.H., Chen, Q., Shi, C. et al. (2021). Dealing with the foreign body response to implanted biomaterials: Strategies and applications of new materials. Adv. Funct. Mater., 31(6): 2007226.
8. Heimann, R.B., Lehmann, H.D. (2015). *Bioceramic Coatings for Medical Implants. Trends and Techniques.* Wiley-VCH, Weinheim. 467 pp. ISBN 978-3-527-334743-9.
9. Brande, W.T., Taylor, A.S. (1863): *Chemistry*. Blanchard and Lea, Philadelphia. 696 pp.
10. Warington, R. Jr. (1866): Researches on the phosphates of calcium, and upon the solubility of tricalcic phosphate. J. Chem. Soc., 19, 296-318.
11. Bragg, W.H. (1921): Application of the ionisation spectrometer to the determination of the structure of minute crystals. Proc. Phys. Soc. (London), 33, 222-224.
12. Hendricks, S.B., Hill, W.A., Jakobs, K.D., Jefferson, M.E. (1931): Structural characteristics of apatite-like substances and composition of phosphate rock and bone as determined from microscopical and X-ray examinations. Ind. Eng. Chem., 23(12), 1413-1418.
13. Roseberry, H.H., Hastings, A.B., Morse, J.K. (1931): X-ray analysis of bone and teeth. J. Biol. Chem., 90, 395-407.
14. Trömel, G. (1932): Untersuchungen über die Bildung eines halogenfreien Apatits aus basischen Calciumphosphaten. Z. Phys. Chem. A, 158, 422-432.

15. Bredig, M.A. (1933): Zur Apatitstruktur der anorganischen Knochen- und Zahnsubstanz. Hoppe-Seyler's Z. Physiol. Chem., 216(5-6), 239-243.
16. Bredig, M.A., Franck, H.H., Füldner, H. (1933): Beiträge zur Kenntnis der Kalk-Phosphorsäure-Verbindungen II. Z. Elektrochem., 39(12), 959-969.
17. De Jong, W.F. (1926): La substance minerale dans les os. Recl. Trav. Chim. Pays-Bas Belg., 45(6), 445-448.
18. De Leeuw, N.H., Bowe, J.R., Rabone, J.A.L. (2007): A computational investigation of stoichiometric and calcium-deficient oxy- and hydroxyapatites. Faraday Discuss., 134, 195-214.
19. Alberius Henning, P., Landa-Canovas, A., Larsson, A.K., Lidin, S. (1999). The structure of oxyapatite solved by HREM. Acta Cryst., B55, 170-176.
20. Calderin, L., Stott, M.J., Rubio, A. (2003). Electronic and crystallographic structure of apatites. Phys. Rev., B67, 134106-134112.
21. Gross, K.A., Pluduma, L. (2012). Putting oxyhydroxyapatite into perspective. A pathway to oxyapatite and its application. In: R. B. Heimann (ed.), *Calcium Phosphate. Structure, Synthesis, Properties, and Applications.* Biochemistry Research Trends Ser., Nova Science Publ., New York, pp. 95-120. ISBN 978-1-62257-299-1.
22. Heimann, R.B. (2009). Characterisation of as-sprayed and incubated hydroxyapatite coatings with high resolution techniques. Mater.-wiss. Werkstofftechn., 40(1-2), 21-30.
23. Hattori, T., Iwadate, Y. (1990). Hydrothermal preparation of calcium hydroxylapatite powders. J. Am. Ceram. Soc., 73, 1803-1807.
24. Liu, C., Huang, A., Shen, W., Cui, J. (2001). Kinetics of hydroxyapatite precipitation at pH 10 and 11. Biomater., 23, 301-306.
25. Rey, C., Combes, C., Drouet, C., Glimcher, M.J. (2009). Bone mineral: update on chemical composition and structure. Osteopor. Int., 20(6), 1013-1021.
26. Pasteris, J.D. (2012). Structurally incorporated water in bone apatite: A cautionary tale. In: R. B. Heimann (ed.), *Calcium Phosphate. Structure, Synthesis, Properties, and Applications.* Biochemistry Research Trends Ser., Nova Science Publ., New York, pp. 63-94. ISBN 978-1-62257-299-1
27. Heimann, R.B. (2020). *Materials for Medical Application*. Walter de Gruyter GmbH, Berlin, Boston, 615 pp, ISBN 978-3-11-061919-5.
28. Glimcher, M.J. (1968). A basic architectural principle in the organisation of mineralized tissue. Clin. Orthop., 61, 16-36.
29. Florencio-Silva, R., Rodrigues da Silva Sasso, G., Sasso-Cerri, E., Simões, M.J., Cerri, P.S. (2015). Biology of bone tissue: structure, function, and factors that influence bone cells. Biomed. Res. Int., 2015: 421746.
30. Allo, B.A., Costa, D.O., Dixon, S.J., Mequanint, K., Rizkalla, A.S. (2012). Bioactive and biodegradable nanocomposites and hybrid biomaterials for bone regeneration. J. Funct. Mater., 5(2), 432-463.
31. Nair, A.K., Gautieri, A., Chang, S.W., Buehler, M.J. (2013). Molecular mechanics of mineralized collagen fibrils in bone. Nature Comm., 4: 1724.
32. Jarcho, M., Bolen, C.M., Thomas, M.B. et al. (1976). Hydroxylapatite synthesis and characterization in dense polycrystalline form. J. Mater. Sci,m 11, 2027-2035; also Jarcho, M. (1981). Calcium phosphate ceramics as hard tissue prosthetics. Clin. Orthop. Rel. Res.,157, 259-278.
33. Ducheyne, P., Hench, L.L., Kagan, A., Martens, M., Mulier, J.C., Burssens, A. (1980). The effect of hydroxyapatite impregnation on bonding of porous coated implants, J. Biomed. Mater. Res., 14, 225-237.
34. Albrektsson, T., Johansson, C. (2001). Osteoinduction, osseoconduction and osseointegration. Eur. Spine J., 10(Suppl. 2), S96-S101.
35. León, B., Jansen, J.A. (2009). *Thin Calcium Phosphate Coatings for Medical Implants*. Springer, New York. 328 pp. ISBN 978-0-387-77718-4.
36. Heimann, R.B. (2008). *Plasma Spray Coating. Principles and Applications*. 2nd. edn., Wiley-VCH, Weinheim. ISBN 978-3-527-32050-9.
37. Heimann, R.B. (2018). Hydroxylapatite coatings: Applied mineralogy research in the bioceramics field. In: S. Heuss-Aßbichler, G. Amthauer, M. John (eds), *Highlights in Applied Mineralogy*, Walter de Gruyter GmbH Berlin, Boston, pp. 301-316. ISBN 978-3-11-049122-7.
38. Sun, L. (2018). Thermal spray coatings on orthopedic devices: When and how the FDA reviews your coatings. J. Thermal Spray Technol., 27, 1280-1290.
39. Graßmann, O., Heimann, R.B. (2000). Compositional and microstructural changes of engineered plasma-sprayed hydroxyapatite coatings on Ti6Al4V substrates during incubation in protein-free simulated body fluid. J. Biomed. Mater. Res., 53(6), 685-693.
40. Heimann, R.B., Graßmann, O., Zumbrink, T., Jennissen, H.P. (2001). Biomimetic processes during *in vitro* leaching of plasma-sprayed hydroxyapatite coatings for endoprosthetic application. Mater.-wiss. Werkstofftechn., 32, 913-921.
41. Dyshlovenko, S., Pateyron, B., Pawlowski, L., Murano, D. (2004). Numerical simulation of hydroxyapatite powder behaviour in plasma jet. Surf. Coat. Technol., 179, 110-117.
42. Riboud, P.V. (1973). Composition et stabilité des phases a structure d'apatite dans le systeme CaO-P_2O_5-oxide de Fer-H_2O a haute temperature. Ann. Chim., 8, 381-390.

43. Frayssinet, P., Tourenne, F., Roquet, N., Conte, P., Delga, C., Bonel, G. (1994). Comparative biological properties of HA plasma-sprayed coatings having different crystallinities. J. Mater. Sci. Mater. Med., 5, 11-17.
44. De Santis, D., Guerriero, C., Nocini, P.F., Ungersbock, A., Richards, G., Gotte, P., Armato, U. (1996). Adult human bone cells from jaw bones cultured on plasma-sprayed or polished surfaces of titanium or hydroxyapatite discs. J. Mater. Sci. Mater. Med., 7(1), 21-28.
45. Ntsoane, T.P., Topić, M., Härting, M., Heimann, R.B., Theron, C. (2016). Spatial and depth-resolved studies of air plasma-sprayed hydroxyapatite coatings by means of diffraction techniques: Part 1. Surf. Coat. Technol., 294, 153-163.
46. Hesse, C., Hengst, M., Kleeberg, R., Götze, J. (2008). Influence of experimental parameters on spatial phase distribution in as-sprayed and incubated hydroxyapatite coatings. J. Mater. Sci. Mater. Med., 19(10), 3225-3241.
47. Park, E., Condrate, R.A., Lee, D.H. (1998). Infrared spectral investigation of plasma spray coated hydroxyapatite. Mater. Lett., 36(1-4), 38-43.
48. Heimann, R.B. (2007). Novel approaches towards design and biofunctionality of plasma-sprayed osteoconductive calcium phosphate coatings for biomedical implants: The concept of bond coats. In: P. J. Pannone (ed.), *Trends in Biomaterials Research*, Nova Science Publishers Inc., USA, pp. 1-80. ISBN 978-1-60021-361-8.
49. Heimann, R.B., Tran, H.V., Hartmann, P. (2003). Laser-Raman and nuclear magnetic resonance (NMR) studies on plasma-sprayed hydroxyapatite coatings: Influence of bioinert bond coats on phase composition and resorption kinetics in simulated body fluid. Mater.-wiss. Werkstofftechn., 34(12), 1163-1169.
50. Kim, H.M., Miyazaki, M., Kokubo, T., Nakamura, T. (2001). Revised simulated body fluid. Key Eng. Mater., 192/195, 47-50.
51. Park, E., Condrate, R.A., Lee, D.H., Kociba, K., Gallagher, P.K. (2002). Characterization of hydroxyapatite before and after plasma spraying. J. Mater. Sci. Mater. Med., 13, 211-218.
52. Demnati, I., Parco, M., Grossin, D. et al. (2012). Hydroxyapatite coating on titanium by a low energy plasma spraying mini-gun. Surf. Coat. Technol., 206, 2346-2353.
53. Demnati, I., Grossin, D., Combes, C., Rey, C. (2014). Plasma-sprayed apatite coatings: Review of physical-chemical aspects and their biological consequences. J. Med. Biol. Eng., 34(1), 1-7.
54. Heimann, R.B., Vu, T.A. (1996). Improvement of adhesion of bioceramic coatings on jaw and bone implants made from titanium alloy. Second Interim Report, SMWK-Projekt No. 7541.82-0390/414. February 15, 1996.
55. Cusco, R., Guitian, F., de Aza, S., Artus, L. (1998). Differentiation between hydroxyapatite and ß-tricalcium phosphate by means of µ-Raman spectroscopy. J. Eur. Ceram. Soc., 18, 1301-1305.
56. Shamray, V.F., Sirotinkin, V.P., Kalita, V.I., Komlev, V.S., Barinov, S.M., Fedotov, A. Yu., Gordeev, A.S. (2019). Studies of the crystal structure of hydroxyapatite in plasma coating. Surf. Coat. Technol., 372, 201-208.
57. Hartmann, P., Jäger, C., Barth, S., Vogel, J., Meyer, K. (2001). Solid state NMR, X-ray diffraction, and infrared characterization of local structure in heat-treated oxyhydroxylapatite microcrystals: An analogy of the thermal deposition of hydroxyapatite during plasma-spray procedure. J. Solid State Chem., 160, 460-468.
58. Jäger, C., Welzel, T., Meyer-Zaika, W., Epple, M. (2006). A solid-state NMR investigation of the structure of nanocrystalline hydroxyapatite. Magn. Reason. Chem., 44, 573-580.
59. Tran, T.H.V. (2004). Investigation into the thermal dehydroxylation and decomposition during atmospheric plasma spraying: NMR and Raman spectroscopic study of as-sprayed coatings and coatings incubated in simulated body fluid. Ph.D. Thesis, Dept. of Mineralogy, Technische Universität Bergakademie Freiberg, Germany.
60. Hartmann, P., Barth, S., Vogel, J., Jäger, C. (2000). Investigation of structural changes in plasma-sprayed hydroxy/apatite coatings. In: Rammlmair, D. et al. (eds)., *Applied Mineralogy in Research, Economy, Technology, Ecology and Culture*. A.A. Balkema, Rotterdam, Brookfield. vol.1, pp. 147-150. ISBN 90-5809-164-3.
61. LeGeros, R.Z. (2001). Formation and transformation of calcium phosphates: Relevance to vascular calcification. Z. Kardiol., 90 (Suppl. 3), 116-124.
62. von Euw, S., Wang, Y., Laurent, G., Drouet, C., Barbonneau, F., Nassif, N., Azais, T. (2019). Bone mineral: New insights into its chemical composition. Sci. Rep., 9(1): 8456.
63. Posner, A.S., Perloff, A., Diorio, A.F. (1958). Refinement of the hydroxyapatite structure. Acta Cryst., 11, 308-309.
64. Heimann, R.B. (2018). Plasma-sprayed hydroxylapatite coatings as biocompatible intermediaries between inorganic implant surfaces and living tissue. J. Thermal Spray Technol., 27(8), 1212-1237.
65. 65.. Laskus, A., Kolmas, J. (2017). Ionic substitution in non-apatitic calcium phosphates. Int. J. Mol. Sci., 18(12), article ID 2542.

66. Graziani, G., Boi, M., Bianchi, M. (2018). A review on ionic substitution in hydroxyapatite thin films. Coatings, 8(8), 269.
67. Trombe, J.C., Montel, C. (1971). Sur la préparation del'oxyapatite phospho-calcique, C. R. Acad. Sci. Paris, 273, 462-465.
68. Takahashi, T., Tanase, S., Yamamoto, O. (1978). Electrical conductivity of some hydroxyapatites. Electrochim. Acta, 23, 369-373.
69. Heimann, R.B., Wirth, R. (2006). Formation and transformation of amorphous calcium phosphates on titanium alloy surfaces during atmospheric plasma spraying and their subsequent *in vitro* performance. Biomater., 27, 823-831.
70. Weng, J., Liu, Q., Wolke, C.D., Zhang, D, de Groot, K. (1997). The role of amorphous phase in nucleating bone-like apatite on plasma-sprayed hydroxyapatite coating in simulated body fluid. J. Mater. Sci. Letters, 16, 335-337.
71. Cook, S.D., Thomas, K.A., Kay, J.F., Jarcho, M. (1988) Hydroxyapatite coated titanium for orthopaedic implant applications. Clin. Orthop., 232, 225-243.
72. Yang, C.Y., Wang, B.C., Chang, E., Wu, J.D. (1995). Bond degradation at the plasma-sprayed HA coating/Ti-6Al-4V alloy interface: An in vitro study. J. Mater. Sci. Mater. Med., 6, 258-265.
73. Lemons, J.E. (1994). Biodegradation and wear of total joint replacements. In: H.U. Cameron (ed.). *Bone Implant Interface*, Mosby: St. Louis, Baltimore, Boston, pp. 307-317.
74. Wintermantel, E., Ha, S.W. (1996). *Biokompatible Werkstoffe und Bauweisen. Implantate für Medizin und Umwelt*. Springer-Verlag: Berlin, Heidelberg, Tokio, p. 225.
75. Li, H., Ma, Y.L., Zhao, Z.C., Tian; Y.L. (2019). Fatigue behavior of plasma sprayed structural-grade hydroxyapatite coating under simulated body fluid. Surf. Coat. Technol., 368, 110-118.
76. Reisel, G., Heimann, R.B. (2004). Correlation between surface roughness of plasma-sprayed chromium oxide coatings and powder grain size distribution: A fractal approach. Surf. Coat. Technol., 185, 215-221
77. Heimann, R.B. (2011). On the self-affine fractal geometry of plasma-sprayed surfaces. J. Thermal Spray Technol., 20(4), 898-908
78. Gentile, F., Tirinato, I., Battista, E., Causa, F., Liberale, C., di Fabrizio, E.M., Decuzzi, P. (2010). Cells preferentially grow on rough substrates, Biomaterials, 31(28), 7205-7212.
79. Gittens, R.A., Olivares-Navarrete, R., Schwartz, Z., Boyan, B.D. (2014). Implant osseointegration and the role of microroughness and nanostructures: Lessons for spine implants, Acta Biomater., 10(8), 3363-3371.
80. Liu, Y., Rath, B., Tingart, M., Eschweiler, J. (2019). Role of implant modification in osseointegration: A systematic review. J. Biomed. Mater. Res., 108(3), 470-484.
81. Heimann, R.B., Kleiman, J.I. (1988). Shock-induced growth of superhard materials. In: H.C. Freyhardt (ed.). *Crystals, Growth, Properties, and Applications*, vol. 11. Springer, Berlin, Heidelberg, New York, London, Paris, Tokyo. pp. 1-73. ISBN 3-540-18602-6.
82. Gill, S.C., Clyne, T.W. (1990). Stress distribution and material response in thermal spraying of metallic and ceramic deposits. Metall. Trans., B21, 377-385.
83. Kuroda, S., Clyne, T.W. (1991). The quenching stress in thermally sprayed coatings. Thin Solid Films, 200(1), 49-66.
84. Kuroda, S., Dendo, T., Kitahara, S. (1995). Quenching stress in plasma sprayed coatings and its correlation with the deposit microstructure. J. Thermal Spray Technol., 4, 75–84.
85. Matejicek, J., Sampath, S. (2001). Intrinsic residual stresses in single splats produced by thermal spray processes. Acta Mater,. 49, 1993-1999.
86. Matejicek, J., Sampath, S. (2003). In situ measurement of residual stresses and elastic moduli in thermal sprayed coatings. Part 1: Apparatus and analysis. Acta Mater., 51(3), 863-872.
87. Stammeier, J.A., Purgstaller, B., Hippler, D., Mavromatis, V., Dietzel, M. (2018). In-situ Raman spectroscopy of amorphous calcium phosphate to crystalline hydroxyapatite transformation. MethodX, 5, 1241-1250.
88. Topíc, M., Ntsoane, T., Hüttel, T., Heimann, R.B. (2006). Microstructural characterisation and stress determination in as-plasma sprayed and incubated bioconductive hydroxyapatite coatings. Suf. Coat. Technol., 201(6), 3633-3641.
89. Heimann, R.B., Ntsoane, T., Pineda-Vargas, C.A., Przybylowicz, W.J., Topíc, M. (2008). Biomimetic formation of hydroxyapatite investigated by analytical techniques with high resolution. J. Mater. Sci. Mater, Med., 19, 3295-3302.
90. Heimann, R.B., Graßmann, O., Hempel, M., Bucher, R., Härting, M. (2000). Phase content, resorption resistance and residual stresses of bioceramic coatings. In: Rammlmair, D. et al. (eds)., *Applied Mineralogy in Research, Economy, Technology, Ecology and Culture*. A.A. Balkema, Rotterdam, Brookfield. vol.1, pp. 155-158. ISBN 90-5809-164-3.
91. Geesink, R.G. (1990). Hydroxyapatite-coated total hip prostheses two-year clinical and roentgenographic results of 100 cases. Clin. Orthop. Relat, Res., 261, 39-58.
92. ISO 12891-2 (2020). *Retrieval and Analysis of Surgical Implants. Part 2: Analysis of Retrieved Surgical Implants*. Int. Org. Stand., Geneva, Switzerland.

93. ISO 13779-2 (2008). *Implants for Surgery-Hydroxyapatite. Part 2: Coatings of Hydroxyapatite*. Int. Org. Stand., Geneva, Switzerland.
94. Heimann, R.B. (2016). Plasma-sprayed hydroxyapatite-based coatings: Chemical, mechanical, microstructural, and biomedical properties. J. Thermal Spray Technol., 25(5), 827-850.
95. Lacombe, R. (2006). *Adhesion Measurement Methods: Theory and Practice*, CRC Taylor & Francis, Boca Raton, USA.
96. Filiaggi, M.J., Coombs, N.A., and Pilliar, R.M. (1991). Characterization of the interface in the plasma-sprayed HApcCoating/Ti-6Al-4V implant system, J. Biomed. Mater. Res., 25, 1211-1229.
97. Webster, T.J., Ergun, C., Doremus, R.H., and W.A. Lanford, W.A. (2003). Increased osteoblast adhesion on titanium-coated hydroxylapatite that forms $CaTiO_3$, J. Biomed. Mater. Res. A, 67(3), 975-980.
98. Wei, D., Zhou, Y., Jia, D., Wang, Y. (2007). Structure of calcium titanate/titania bioceramic composite coatings on titanium alloy and apatite deposition on their surfaces in a simulated body fluid, Surf. Coat. Technol., 201, 8715-8722.
99. Joshi, M.U., Kulkarni, S.P., Choppadandi, M. et al. (2023). Current state of art smart coatings for orthopedic implants: A comprehensive review. Smart Mater. Med., 4, 661-679.